ACS OMEGA

Open Access

http://pubs.acs.org/journal/acsodf

Article

Interfacial Engineering over Pt−Calcium Ferrite/2D Carbon Nitride Nanosheet p−n Heterojunctions for Superior Photocatalytic Properties

Rajendra V. Singh, Mrinal R. Pai,* Atindra M. Banerjee, Anshu Shrivastava, Uttam Kumar, Indrajit Sinha, Bijaideep Dutta, Puthusserickal A. Hassan, Raghumani S. Ningthoujam, Rajib Ghosh, Sukhendu Nath, Rajendra K. Sharma, Jagannath, and Rudheer D. Bapat

Cite This: *ACS Omega* 2024, 9, 40182−40203

Read Online

ACCESS | Metrics & More | Article Recommendations | Supporting Information

ABSTRACT: The present study discloses the fabrication of efficient p−n heterojunctions using n-type polymeric bulk carbon nitride (b-CN, E_g = 2.7 eV) or exfoliated nanosheets of carbon nitride (NSCN, E_g = 2.9 eV) with p-type spinel ferrite $CaFe_2O_4$ (CFO, E_g = 1.9 eV) for photocatalytic hydrogen generation. A series of p−n combinations were fabricated and characterized by various techniques. The oxide−carbon nitride interactions, light absorption, band alignment at the interface, and water/H_3O^+ adsorption capability were elucidated over heterojunctions and correlated with the photocatalytic hydrogen yield. The main developments in the present study are as follows: (1) All heterojunctions were more active than pure phases. (2) The photocatalytic activity trend validated an increase in the lifetime of charge carriers from TRPL. Pt(1 wt %)−CFO(1 wt %)/NSCN (481.5 μmol/h/g under ultraviolet (UV)−visible-simulated light, 147.5 μmol/h/g under CFL illumination for 20 h, τ_{avg} = 10.33 ns) > Pt−NSCN > Pt−CFO/b-CN > CFO/NSCN > CFO/b-CN > NSCN > Pt/b-CN > mechanical mixture (MM) of 1 wt %CFO + NSCN−MM > 1 wt %CFO + b-CN−MM > CFO > b-CN (τ_{avg} = 4.5 ns). (3) Pt−CFO/NSCN was most active and exhibited 250 times enhanced photocatalytic activity as compared to parent bulk carbon nitride, 6.5 times more active than CFO/NSCN, and twice more active than Pt−NSCN. Thus, enhanced activity is attributed to the smooth channelizing of electrons across p−n junctions. (4) NSCN evidently offered improved characteristics as a support and photocatalyst over b-CN. The exfoliated NSCN occupied a superior few-layer morphology with 0.35 nm width as compared to parent b-CN. NSCN allowed 57% dispersion of 6 nm-sized CFO, while b-CN supported 14% dispersion of 7.8 nm-sized CFO particles, as revealed by small-angle X-ray scattering spectroscopy (SAXS). Sizes of 2−4 nm were observed for Pt nanoparticles in the 1 wt %Pt/1 wt % CFO/NSCN sample. A binding energy shift and an increase in the FWHM of X-ray photoelectron spectroscopy (XPS) core level peaks established charge transfer and enhanced band bending on p−n contact in Pt−CFO/NSCN. FsTAS revealed the decay of photogenerated electrons via trapping in shallow traps (τ_1, τ_2) and deep traps (τ_3). Lifetimes τ_1 (3.19 ps, 42%) and τ_2 (187 ps, 31%) were higher in NSCN than those in b-CN (τ_1 = 2.2 ps, 42%, τ_2 = 30 ps, 31%), which verified that the recombination reaction rate was suppressed by 6 times in NSCN ($k_2 = 0.53 \times 10^{10}$ s^{-1}) as compared to b-CN ($k_2 = 3.33 \times 10^{10}$ s^{-1}). Deep traps lie below the H^+/H_2 reduction potential; thus, electrons in deep traps are not available for photocatalytic H_2 generation. (5) The role of CFO in enhancing water adsorption capability was modeled by molecular dynamics. NSCN or b-CN both showed very poor interaction with water molecules; however, the CFO cluster adsorbed H_3O^+ ions very strongly through the electrostatic interaction between calcium and oxygen (of H_3O^+). Pt also showed a strong affinity for H_2O but not for H_3O^+. Thus, both CFO and Pt facilitated NSCN to access water molecules, and CFO further sustained the adsorption of H_3O^+ molecules, crucial for the photocatalytic reduction of water molecules. (6) Band potentials of CFO and NSCN aligned suitably at the interface of CFO/NSCN, resulting in a type-II band structure. Valence band offset (VBO, ΔE_{VB}) and conduction band offset (CBO, ΔE_{CB}) were calculated at the interface, resulting in

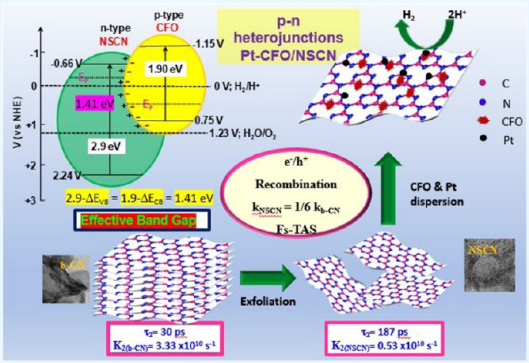

continued...

Received: July 9, 2024
Revised: August 3, 2024
Accepted: August 8, 2024
Published: September 9, 2024

an effective band gap of 1.41 eV ($2.9 - \Delta E_{VB} = 1.9 - \Delta E_{CB}$), much lower than parent compounds. The interfacial band structure was efficient in driving photogenerated electrons from the CB of CFO to the CB of NSCN and holes from the VB of NSCN to the VB of CFO, thus successfully separating charge carriers, as supported by the increased lifetime of charge carriers and favorable photocatalytic H_2 yield.

1. INTRODUCTION

Photocatalytic water splitting, analogous to photosynthesis, is a potential process for harvesting sunlight into chemical energy.[1] The historical experiment by Honda and Fujishima in 1972[2] led to vigorous research in photoelectrochemical, electrocatalytic, or photocatalytic splitting of water. All these processes are dependent on active and stable photocatalysts or electrocatalysts for efficient water splitting. In pursuit of effective and sustainable photocatalysts, researchers from all over the world have investigated several categories of materials, starting from traditional photocatalysts belonging to oxides, sulfides, selenides, such as TiO_2, CdS, CdSe, WO_3, etc.,[3−5] further to nitrides, carbides, oxynitrides, oxysulfides, etc.,[6−9] in different morphologies, namely, nanowires, nanotubes, nanoparticles, powder, thin films,[10,11] etc. However, issues such as poor visible light absorption, photocorrosion, fast e^-/h^+ recombination, and poor catalytic activity are associated with these reported studies, and a perfect photocatalyst exhibiting ideal properties is yet to be formulated.

Polymeric assemblies based on heptazine, triazine, porphyrin, benzene, etc., moieties, inherently possessing strong conjugated systems, high surface areas, and porosity, have gained tremendous attention during the past few years. Graphitic carbon nitride (g-C_3N_4) is an organic conjugated semiconductor with heptazine rings that has shown tremendous potential for energy, anticancer, sensors, and other applications.[12] g-C_3N_4 is a metal-free polymeric, n-type, low-band-gap (E_g = ∼2.7 eV), stable semiconductor, having unique electric, optical, structural, and physicochemical properties.[13−17] Wang et al. in 2009[13] revealed its potential for direct water splitting, and subsequently, carbon nitride-based photocatalysts were extensively investigated.[18−22] Wen et al.[21] reviewed these multifunctional nitrides and revealed how these classes of compounds have gained popularity at par with TiO_2 during the past decade for their performance in photocatalytic reactions related to environment and energy applications. However, with respect to photocatalytic hydrogen generation, carbon nitride suffers from limitations of fast e^-/h^+ recombination and limited visible light absorption. To improve its electronic and optical properties, various modifications such as nanoarchitecture design, exfoliation, functionalization at an atomic level leading to cationic/anionic doping, molecular-level copolymerization, heterojunction formation with other semiconductors, dispersion of metals, dye sensitization, etc., were attempted.[13,23−26] Two-dimensional (2D) nanosheets drawn from layered bulk carbon nitride are superior hosts for heterojunctions. 2D nanosheets offer a high surface area to accommodate a large number of active sites and shorten the diffusion length for charge carriers, a reduced rate of the recombination reaction, and improved photocatalytic activity.[27] Using femtosecond transient absorption spectroscopy (FsTAS), we have shown in the present study that 2D nanosheets allow fast migration and separation of charge carriers compared to bulk carbon nitride. Although 2D nanosheets display superior properties, they still suffer from weak static internal electric fields attributed to highly symmetrical unit cells. To overcome these static forces and to fasten the charge transfer dynamics, heterojunctions with other semiconductors or metal ions are a very effective strategy.

Carbon nitride-based heterojunctions have shown their capability for environmental remediation, energy storage, photocatalytic reactions, biosensors, etc.[13−17,27−29] Heterojunctions formed between two semiconductors with appropriate band positions allow smooth channeling of photogenerated charge carriers and expand the light absorption range. It is an unfailingly proven methodology for enhancing photocatalytic properties. For heterojunctions, it is important that both p- and n-type semiconductors have appropriate band potentials. As p- and n-type semiconductors are brought into contact, electrons and holes flow in opposite directions until the Fermi level equilibrates, the VB and CB of both semiconductors align at the interface, and an internal electric field is induced, leading to the accumulation of charges and space charge layer formation. After contact, the offset between the conduction bands and valence bands of the two semiconductors at the interface effectively reduces the band gap of the composite material. A large number of heterojunctions[27−29] are investigated using state-of-the-art or modified carbon nitrides, such as CdS/g-C_3N_4,[30] Bi_2S_3/g-C_3N_4,[31] $Mn_{0.5}Cd_{0.5}Se$/g-C_3N_4,[32] RuO_2/α-Fe_2O_3/g-C_3N_4,[33] etc., for photocatalytic water splitting.

We have recently reported superior photocatalytic properties of Schottky junctions prepared by dispersing metal (Pt, Pd, Ag, Au, and Cu) nanoparticles on g-C_3N_4.[34] Here, metal−support interactions, band alignment at the interface, and charge transfer kinetics of photogenerated electrons from the CB of g-C_3N_4 to active sites of metal nanoparticles were investigated and correlated with enhanced photocatalytic activity. Earlier also, we reported a detailed investigation on NiO−TiO_2 p−n heterojunctions designed to yield highly efficient and sustainable hydrogen generation as compared to pristine parent oxides.[35]

Spinel, calcium ferrite, $CaFe_2O_4$ (CFO), a p-type magnetic semiconductor with a low band gap typically of 1.9 eV, has been reported previously for various applications as p-type photoelectrodes,[36] photocatalysts,[37] solid catalysts,[38] and electrodes for solid oxide fuel cells.[39] Calcium ferrite is advantageous for enhancing visible light absorption, is easily separable due to being magnetic, and has a simple scalable preparation process from low-cost, abundantly available elements. Investigations on $CaFe_2O_4$/g-C_3N_4 heterojunctions are very few and that too are mainly reported for photocatalytic degradation of toxins and contaminants present in water as pollutants.[40−47]

The present study focuses on the engineering of p−n heterojunctions between two-dimensional exfoliated carbon nitride nanosheets or bulk carbon nitride and spinel calcium ferrite along with Schottky junctions using Pt nanoparticles. We report here an in-depth, comprehensive study investigating synthesis, characterization, and modified optical, electronic, water adsorption, and photocatalytic properties before and after the formation of heterojunctions. Band gap alignment/band potentials/offsets, lifetimes, and kinetics of charge carriers at the interface, and spinel−metal−support interactions in nano-heterojunctions are reported and correlated with improved photocatalytic properties. Phase pure compound bulk g-C_3N_4, nanosheets of g-C_3N_4, and $CaFe_2O_4$ were synthesized by

https://doi.org/10.1021/acsomega.4c06353
ACS Omega 2024, 9, 40182−40203

thermal pyrolysis of nitrogen-rich precursors, acid-mediated exfoliation, and the Pechini method, respectively. p−n nanoheterojunctions between p-type $CaFe_2O_4$ and n-type bulk and nanosheets of g-C_3N_4 were fabricated using solvothermal synthesis. Active sites were created by dispersing Pt nanoparticles onto the heterojunctions. Phase identification and the structure of heterojunctions as well as control samples were identified by recording X-ray diffraction (XRD) and Fourier transform infrared spectroscopy (FTIR). The chemical composition of different components in heterojunctions was confirmed by inductively coupled plasma optical emission spectrometry (ICP-OES) and element dispersive X-ray (EDX). Modification in optical properties, particularly visible light absorption and band gap, along with shallow trap states at the interface, was investigated by recording ultraviolet (UV)−visible diffuse reflectance spectra (DRS). The nature of linkages existing between two different semiconductors and metal nanoparticles dispersed on nanosheets as a support was established by X-ray photoelectron spectroscopy (XPS), photoluminescence spectra (PL), and Mott−Schottky (M−S) analysis. Morphology, particle size, and extent of dispersion were probed by small-angle X-ray scattering spectroscopy (SAXS), scanning electron microscopy (SEM) selected area electron diffraction (SAED) in low resolution (LR), and high-resolution transmission electron microscopy (HRTEM). The relative distribution of the $CaFe_2O_4$ phase and Pt nanoparticles in the Pt/$CaFe_2O_4$/nanosheet heterojunction was examined by recording high−angle annular dark−field scanning transmission electron microscopy (HAADF-STEM) images and conducting X-ray mapping over a selected area in these images. The role of nanosheets in improving the charge transfer kinetics of photogenerated electrons compared to bulk carbon nitride was investigated by femtosecond transient absorption spectroscopy (FsTAS). The lifetime of charge carriers at the interface of p−n heterojunctions was monitored in the nanosecond regime by time-resolved photoluminescence spectroscopy (TRPL). Photocatalytic hydrogen yield was evaluated over all nanoheterojunctions, such as CFO/b-CN, CFO/NSCN, Pt−CFO/b-CN, Pt−CFO/NSCN, Pt−NSCN, Pt−b-CN, corresponding mechanical mixtures, and parent samples, under UV−visible and exclusively visible CFL irradiation. In any catalytic mechanism, adsorption is the foremost important and rate-determining step. The interaction of pristine carbon nitride with water molecules is very poor, and to understand the role of CFO and Pt in enhancing the adsorption capabilities of carbon nitride nanosheets toward water and H_3O^+ ions, theoretical simulations using classical molecular dynamics were conducted. Four models were simulated to investigate the interaction of H_2O molecules and H_3O^+ ions with different composites of a g-C_3N_4 nanosheet and other components, namely, CFO and Pt.

2. EXPERIMENTAL SECTION

Carbon nitride was prepared by the most commonly used thermal pyrolysis of nitrogen precursors, such as urea, melamine, etc. In the present study, melamine was placed in a covered cylindrical alumina crucible to maintain a semiclosed environment and heated in a muffle furnace at 550 °C for 2 h to yield yellow-colored bulk carbon nitride, referred to here as b-CN. It is a layered compound that was further exfoliated into nanosheets, NSCN, by adopting a sulfuric acid-mediated approach. A pure phase of $CaFe_2O_4$ (CFO) was prepared by the sol−gel based Pechini method. 1 wt % CFO was dispersed on bulk and nanosheets of carbon nitride to form $CaFe_2O_4$/g-C_3N_4 heterojunctions abbreviated as CFO/CN and CFO/NSCN, respectively. 1 wt % Pt was dispersed over photocatalysts by the photodeposition method, leading to Pt−CFO/b-CN (or NSCN) heterojunctions. A schematic of the syntheses of parent compounds and heterojunctions is provided in Figure S1, and synthetic protocols are explained in detail in the Supporting Information, S1. Henceforth, the above-mentioned abbreviations will be used to refer to the photocatalyst samples in the present manuscript. XRD, FTIR, ICP-OES, UV−visible DRS, PL, Mott−Schottky analysis, VBM-XPS, XPS, SAXS, SEM, SAED-TEM-HRTEM, TRPL, and FsTAS techniques were utilized for characterization. Photocatalytic hydrogen yield was evaluated over 50 to 80 mg of nanoheterojunctions, CFO/b-CN and CFO/NSCN, along with control samples in the presence of triethanolamine under UV−visible and exclusively visible CFL irradiation. H_2 yield was quantified using gas chromatography equipped with a molecular sieve capillary column and a thermal conductivity detector. To understand the role of CFO and Pt in enhancing the adsorption capabilities of carbon nitride nanosheets toward water and H_3O^+ ions, theoretical simulations using classical molecular dynamics were performed. The details about experiments, including emission spectra, photocatalytic reactors, characterization techniques, and theoretical simulations are provided in the Supporting Information, S1.

3. RESULTS AND DISCUSSION

3.1. Photocatalytic Activity under Simulated Sunlight and CFL. The photocatalytic activities of all samples, including bulk carbon nitride, exfoliated nanosheets of b-CN, CFO dispersed on both bulk and nanosheets, namely, CFO/b-CN and CFO/NSCN, Pt nanoparticles dispersed over photocatalysts, namely, Pt−b-CN and Pt−NSCN, and heterostructures of Pt−CFO/NSCN and Pt−CFO/b-CN, were evaluated under different light sources and experimental conditions (Table 1).

The amount of photocatalytic hydrogen evolved with time under simulated UV−visible irradiation over different photocatalysts is shown in Figure 1a. Parent b-CN showed poor H_2 evolution@1.9 μmol/h/g, which on exfoliation into nanosheets escalated to 66 μmol/h/g in NSCN. The p-type CFO pure phase, despite having the lowest band gap, exhibited a poor hydrogen evolution rate, typically ∼0.8 μmol/h over 50 mg of the photocatalyst or ∼17 μmol/h/g under UV−visible light. However, dispersion of 1 wt % CFO on b-CN or NSCN resulted in a considerable increase in H_2 yield due to the formation of p−n heterojunctions between p-type CFO and n-type carbon nitride bulk or nanosheets as CFO/b-CN and CFO/NSCN, respectively. Dispersion of Pt as a cocatalyst provided active sites for the photocatalytic hydrogen evolution reaction and further improved the H_2 yield to a greater extent. The performance of the Pt(1 wt %)−CFO(1 wt %)/NSCN nanocomposite was found to be superior to all other samples with a H_2 evolution rate of 481.5 μmol/h/$g_{(catalyst)}$ or 530 μmol/h/$g_{(NSCN)}$ or 48150 μmol/h/$g_{(CFO)}$ under UV−visible light. The trend of photocatalytic activity under UV−visible-simulated light was found to be Pt-CFO/NSCN> Pt−NSCN > Pt−CFO/b-CN > CFO/NSCN > CFO/b-CN > NSCN > Pt−b-CN > mechanical mixture (MM) of 1 wt % CFO + NSCN−MM > 1 wt % b-CN + CFO−MM > CFO > b-CN (Figure 1 and Table 1). The rate of H_2 generated over different samples is compared using a bar graph in Figure 1b. Pt−CFO/NSCN exhibited 250 times more activity as compared to bulk carbon nitride, 6.5 times more active than CFO/NSCN, 7 times more active than NSCN, and

https://doi.org/10.1021/acsomega.4c06353
ACS Omega 2024, 9, 40182−40203

Table 1. Comparison of Photocatalytic H_2 Yield over p−n Heterojunctions Compared to Control Samples under Various Irradiation Sources

	activity (μmol/h/$g_{catalyst}$)		activity (μmol/h/$g_{CFO\ or\ Pt}$)		[c]
sample	simulated UV−vis light[a] (A)	visible light from CFL[b]	simulated UV−vis light	visible light from CFL	ratio[c] A/(1.92)
b-CN	1.92	nil			1
NSCN	66.2				34.5
CFO	17.3		17.3		9.01
CFO/b-CN	63.2		6320		32.9
CFO/NSCN	74.1		7410		38.5
Pt/CFO/b-CN	193.1	72.9	19,310	7290	100.5
Pt/NSCN	221		22,100		115
Pt/CFO/NSCN	481.5	147.5	48,150	14,750	250.7

[a]50 mg of the catalyst was suspended in 15 mL of 10% v/v aqueous triethanolamine in an 81 mL photoreactor having a 20 cm^2 illumination area, irradiated using a 400 W medium-pressure Hg lamp. [b]80 mg of the catalyst was suspended in 150 mL of 10% v/v aqueous triethanolamine in a 2 L photoreactor having a 172 cm^2 illumination area, irradiated using an in-house designed and fabricated visible light irradiation setup based on CFLs. [c]Ratio was calculated using photocatalytic activities of samples expressed in μmol/h/$g_{catalyst}$ given in column 2 (A) under simulated UV−visible light divided by photocatalytic H_2 yield over b-CN under UV−visible light (1.92 μmol/h/$g_{catalyst}$).

~twice as active as Pt−NSCN. (Table 1). Thus, both p−n heterojunctions and metal Schottky junctions contributed to the enhancement of the photocatalytic activity.

Since the main objective is to investigate the solar harvesting capability of these photocatalysts, the viability of these photocatalyst samples was established by testing under visible light irradiation exclusively. Thus, the light source was changed from a UV−visible medium-pressure mercury lamp to CFL irradiation. CFL exhibits emission in the visible region with prominent peaks appearing at 550 nm and above 600 nm.[48] Two most active samples, namely, Pt−CFO/NSCN and Pt−CFO/b-CN heterojunctions, were selected from previous photocatalytic experiments under UV−visible light. The performance of these heterojunctions was further tested in an upscaled photoreactor (2 L capacity) under an in-house fabricated CFL-based irradiator, as shown in Figure 1c. Both samples were found to be active, and the maximum H_2@147 μmol/g/h was demonstrated by Pt−CFO/NSCN as compared to 72 μmol/h/g over Pt−CFO/b-CN (Figure 1c) under visible light emitted by CFLs for a period of 20 h. Hydrogen yield increased linearly with the irradiation time. No evolution of hydrogen gas was detected in the dark. Evacuation or purging of inert gas to remove air/O_2 present in the photoreactor before irradiation is favorable to obtain the maximum hydrogen yield.[49]

The XRD pattern of the spent heterojunction is compared with the fresh sample in the Supporting Information (Figure S2), indicating that these p−n heterojunctions are stable after use for 20 h. In order to confirm that the enhancement in hydrogen evolution is attributed to p−n heterojunctions, a mechanical mixture (MM) of 1 wt % CFO with b-CN and NSCN was prepared and evaluated for photocatalytic hydrogen generation. CFO/b-CN−MM and CFO/NSCN−MM both showed meager activity as compared to the solvothermal fabricated heterojunctions (Figure 1b). The above results clearly indicate that formation of p−n heterojunctions between spinel ferrite and CN or NSCN is responsible for the rise in H_2 yield via smooth channeling and separation of photogenerated e^-/h^+ pairs at the interface. At the same time, CFO participated in the expansion of the light absorption properties of carbon nitride toward the visible region in CFO/b-CN and CFO/NSCN samples. Thus, p−n heterojunctions indeed enhanced the solar light harvesting capabilities. The CFO/b-CN sample demonstrated activity after an activation period of 5 h; however, nanosheets were active under CFL irradiation without any delay. This behavior can be explained by the role of thin sheets of NSCN in improving the charge transfer kinetics (as investigated by FsTAS in subsequent sections), driving photogenerated e^-s at the surface and facilitating their participation in redox processes taking place at active sites. The presence of Pt nanoparticles as active sites/cocatalysts on the surface distinctly enhanced the photoreduction of H_2O to H_2 and provided a well-formed linear hydrogen generation curve. Pt nanoparticles build the passage in the form of Schottky junctions at the interface of CN through which photogenerated electrons are thrust to the surface from bulk, as explained in detail in our recent publication.[34]

3.2. Phase Identification. The XRD patterns of b-CN and exfoliated NSCN are shown in Figure S3a in the Supporting Information. The two characteristic peaks of b-CN appeared at 12.9 and 27.7°, in agreement with JCPDS card No. 87−1526. The low angle peak at 12.9° is attributed to an in-plane structural packing motif of tri-s-triazine units with an interplanar distance of 0.675 nm, while the peak at 27.7° appears from the stacking of aromatic systems with a *d* spacing (interlayer) of 0.321 nm.[50] NSCN was prepared by acid-mediated chemical exfoliation, in which H_2SO_4 molecules were intercalated between layers of b-CN. Sulfuric acid is a strong oxidizing agent and is capable of cleaving the hydrogen bonds existing between two layers. Intercalation of H_2SO_4 between layers of b-CN was obvious from the drastic fall in the intensity of the interlayer stacking peak at 27.7° (Figure S3a). Thus, after exfoliation with H_2SO_4, a broad XRD peak with decreased intensity at nearly the same position of 27.7° was observed (Figure S3a). It is obvious that the number of layers contributing to the interlayer stacking will decline, leading to the few-layer morphology accompanied probably by an increase in the distance between two layers.[51] Similarly, there will be a decreased planar size of g-C_3N_4 layers, and thus, the intensity of the 12.9° peak will also decrease on exfoliation.[51] Thus, a decrease in the intensity of XRD peaks reveals that bulk carbon nitride, b-CN, is exfoliated into nanosheets, NSCN. The XRD pattern of CFO prepared by the Pechini method, calcined successively at 800 and 850 °C, matched with the pure orthorhombic phase of $CaFe_2O_4$ (ICSD Collection Code: 166065) with the space group *Pnma* and unit cell parameters of a = 9.230 Å, b = 10.70 Å, and c = 3.024 Å.[52] The most intense reflection in CFO was due to the 302 plane, hkl_{302}, appearing at 33.6°. 1 wt % CFO was dispersed on NSCN and b-CN by a solvothermal method to form p−n nano-heterojunctions. Weak peaks due to CFO along with peaks due to b-CN and NSCN coexisted in the CFO/b-CN and CFO/NSCN samples, respectively (Figure S3b). A slight decrease in the 2θ values (by 0.25°) was observed in the peak due to the interlayer stacking of NSCN (27.7°) on formation of the CFO/NSCN (27.45°) heterojunction. An increase in the *d* spacing of interlayer stacking suggested inclusion of CFO spinel molecules between two layers of NSCN.[42]

The IR spectra of all samples are given in Figure S4, showing characteristic peaks in the fingerprint region of heptazine

https://doi.org/10.1021/acsomega.4c06353
ACS Omega 2024, 9, 40182−40203

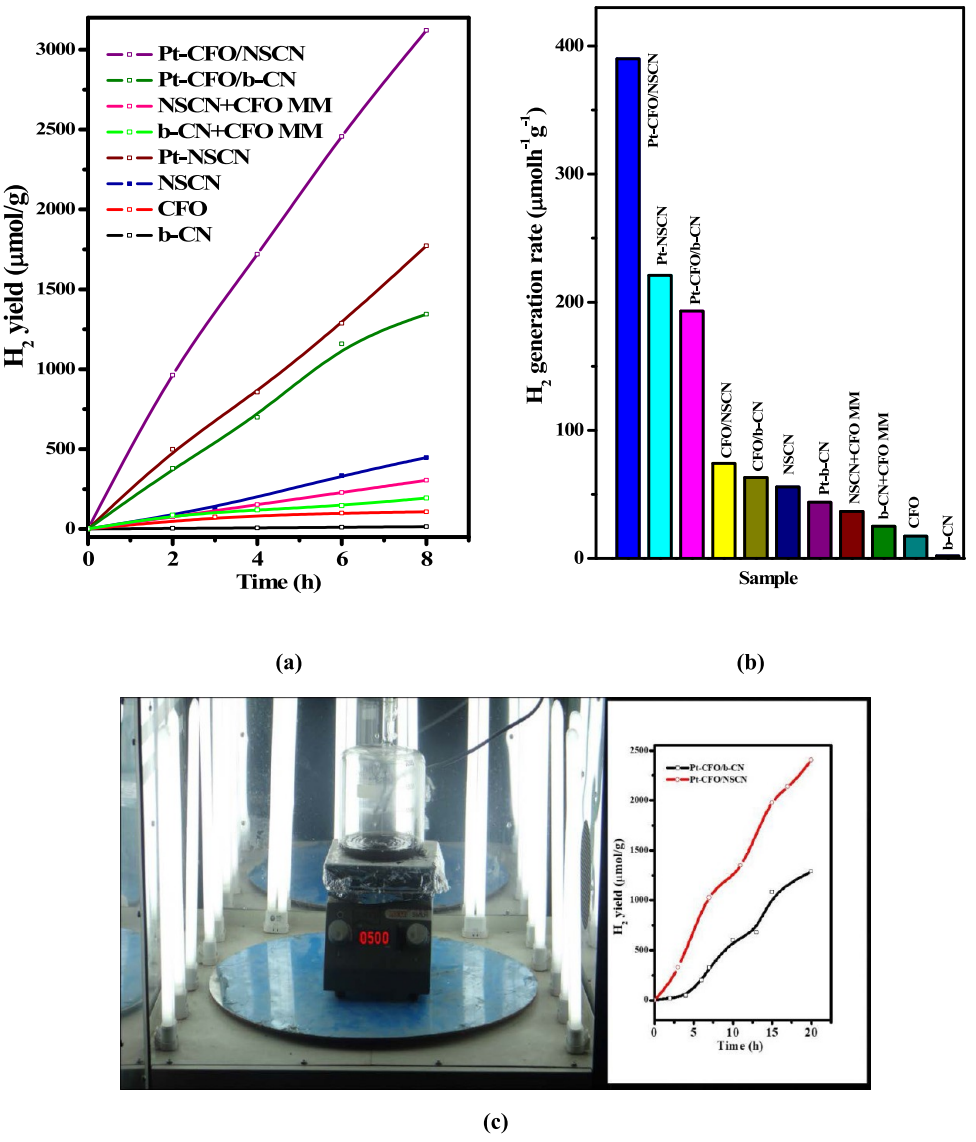

Figure 1. (a) Photocatalytic H_2 yield at different time durations under UV−visible light irradiation in an 81 mL quartz photoreactor. (b) Bar graph comparison and (c) photocatalytic H_2 yield under visible light CFL irradiation for most active samples recorded for 20 h. A photograph of the experimental setup for evaluation of photocatalytic activity in an upscaled photoreactor of 2 L capacity illuminated under an in-house designed CFL-based visible light photoirradiator is also shown.

heterocyclic rings consisting of basic C_6N_7 units appearing at 1000−1750 cm^{-1} and free NH_2 or ═NH groups manifested in the range of 3100−3500 cm^{-1}. The IR spectra of b-CN were modified on exfoliation. The peak at 807 cm^{-1} is attributed to the ring-sextant out-of-plane bending vibration of the triazine or heptazine units.[53] Shifts in this peak by ∼6 and 13 cm^{-1} toward lower wavenumbers were observed in the case of NSCN and CFO/NSCN, respectively, confirming exfoliation.[54] Further, an increase in the intensity of the band at 782 cm^{-1}, which is a typical peak for bending and stretching vibrations of the melamine type of C−N heterocycles, confirms exfoliation.[53]

3.3. Morphology and Composition. The SEM-EDX images of all synthesized photocatalyst samples are shown in Figure S5(a−f). The first three images belong to single-phase parent samples b-CN, NSCN, and CFO, while the last SEM image belongs to the CFO/NSCN composite in which 1 wt % CFO is dispersed on NSCN. The SEM image of b-CN appears to be an amorphous structure with micron-sized particles. Most of the particles had multiple stacked layers and rough surfaces. Further, after exfoliation to NSCN, SEM shows a different structure consisting of micrometer-sized rods with a large number of pores, rougher and etched surfaces. The SEM of calcium ferrite (CFO) has confirmed the presence of agglomerated anisotropic particles. On dispersion of CFO on NSCN by the solvothermal method, SEM has shown that the overall porosity of the photocatalyst has enhanced. EDX spectra were also recorded along with SEM.

The composition of all samples was investigated using different techniques such as CHN, EDX, and ICP-OES, and the analysis results are tabulated in Table 2. Most of the analysis shows that the observed values are close to the expected value. The N/C ratios in b-CN and NSCN were found to be nearly ∼1.49, as against the expected ratio of 1.33 for g-C_3N_4 (Table 2). Although N/C remained almost constant for both b-CN and exfoliated NSCN, mol % of both carbon and nitrogen decreased on exfoliation. The molar concentration of H increases drastically on exfoliation, from 2.7 in b-CN to 3.77 in NSCN (Table 2). In fact, all samples with NSCN as a support show

https://doi.org/10.1021/acsomega.4c06353
ACS Omega 2024, 9, 40182−40203

Table 2. Bulk Chemical Composition, Particle Size Distribution, and Dispersion in Different Samples by Various Techniques[a]

sample	C (mol %)	N (mol %)	H (mol %)	Ca (mol %)	Fe (mol %)	N/C		Fe/Ca		particle size distribution from SAXS[b]	relative dispersion (%) from SAXS[c]
	CHN	CHN	CHN	ICP-OES	ICP-OES	CHN	ideal	ICP-OES	ideal		
b-CN	2.94	4.4	2.7			1.49	1.33				
NSCN	2.23	3.32	3.8			1.48	1.33				
CFO				0.17	0.44			2.28	2		
CFO/b-CN	2.9	4.2	3.0							7.8, 13.2, and 23.7	14
CFO/NSCN	2.3	3.4	3.7	0.01	0.011	1.47	1.33	1.11	2	6, 12.1, and 35.2	57

[a]Ca and Fe from ICP-OES analysis and C, H, and N from a CHNS analyzer. [b]Broad SAXS peaks in CFO/b-CN and CFO/NSCN were deconvoluted. The peak area of deconvoluted peaks and the total peak area are mentioned in the inset of Figure 4c,d. [c]Relative dispersion (%) is defined here as 100 multiplied by the ratio of the volume of CFO particles having sizes less than 7−8 nm/total volume of CFO particles present in the sample. It is assumed that the bigger particles (>10 nm) are in the agglomerated form, which are not available on the surface of carbon nitride for photocatalysis.

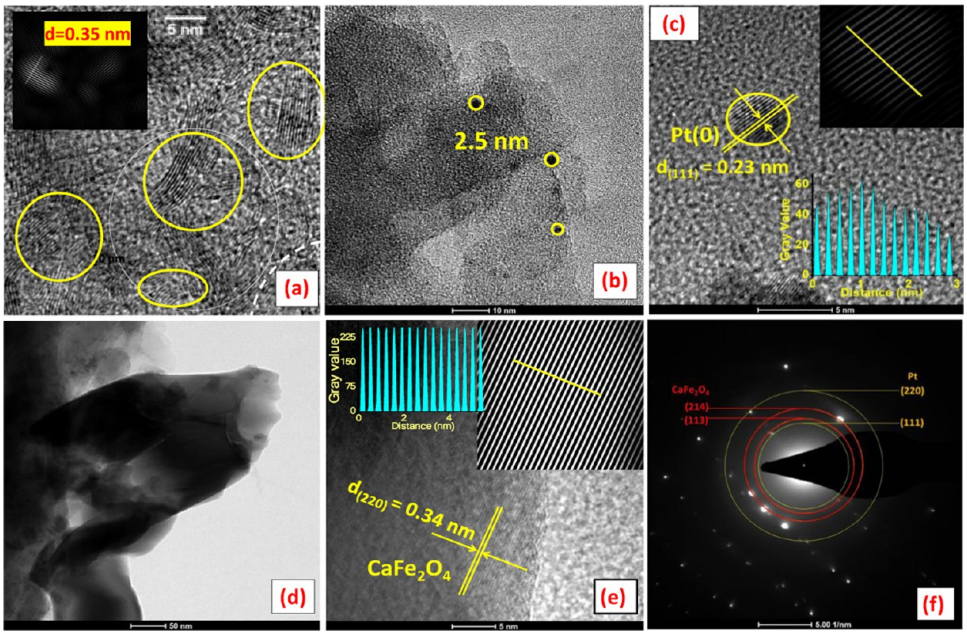

Figure 2. High-resolution TEM images of parent NSCN (a) and Pt−CFO/NSCN (b−e). Selected area electron diffraction (SAED) pattern of Pt−CFO/NSCN (f).

higher concentrations of H atoms due to the higher content of −C−NH_2 uncondensed moieties resulted on exfoliation.[54] The ratio of Fe/Ca in phase pure CFO was found to be 2.28 from ICP-OES, matched with the ideal value of 2, corresponding to the molecular formula of $CaFe_2O_4$. However, the ICP-OES analysis of CFO/NSCN revealed an Fe/Ca ratio of 1.11, much lower than the expected ideal value of 2. A very small amount of CFO (1 wt %) was dispersed on NSCN, so sampling issues can account for these anomalies.

Low-resolution TEM images of b-CN (Figure S5g,h) and NSCN (Figure S5i) reveal the distinct morphologies of both b-CN and NSCN. A characteristic layered structure in which layers are folded at the corners is observed in the images of bulk carbon nitride, while the morphology of NSCN is quite different from b-CN. The high-resolution TEM image of NSCN (Figure 2a) clearly showed a few-layer morphology in contrast to the multilayered morphology of b-CN. Thus, condensed layers of b-CN were reduced to few layers, and the width of individual layers was estimated to be 0.35 nm in NSCN (Figure 2a).

The morphology of different phases coexisting in the nanoheterojunctions of Pt−CFO/NSCN was examined in depth by various imaging and non-imaging techniques. The HRTEM image of Pt−CFO/NSCN (Figure 2b) revealed that 2−3 nm-sized black dots were uniformly distributed on loosely bound layers of carbon nitride nanosheets. On further magnification over black dots, lattice fringes with a *d* spacing of 0.23 nm were observed, which were attributed to the 111 plane of Pt metal (Figure 2c). The presence of calcium ferrite particles with an average size of 10−15 nm was also evident in the adjacent zone of the HRTEM image (Figure 2d). Lattice fringes with a *d* spacing of 0.34 nm were derived using the FFT pattern (Figure 2e) and were attributed to the 220 plane of CFO. The SAED pattern of Pt−CFO/NSCN involved both dotted and diffused rings. Dotted rings were indexed to the 214 and 113 planes of the nanocrystalline orthorhombic CFO phase (Figure 2f), while diffused rings in the SAED pattern were attributed to 220 and 111 planes of Pt nanoparticles.

Thus, the microscopic investigation confirmed that Pt and CFO nanoparticles coexisted uniformly on the surface of nanosheets, NSCN suggesting fabrication of p−n nano-heterojunctions.

To investigate the distribution of Pt and CFO phases on NSCN, HAADF-STEM images were recorded (Figure 3). Pt nanoparticles represented by tiny circular bright spots are more

https://doi.org/10.1021/acsomega.4c06353
ACS Omega 2024, 9, 40182−40203

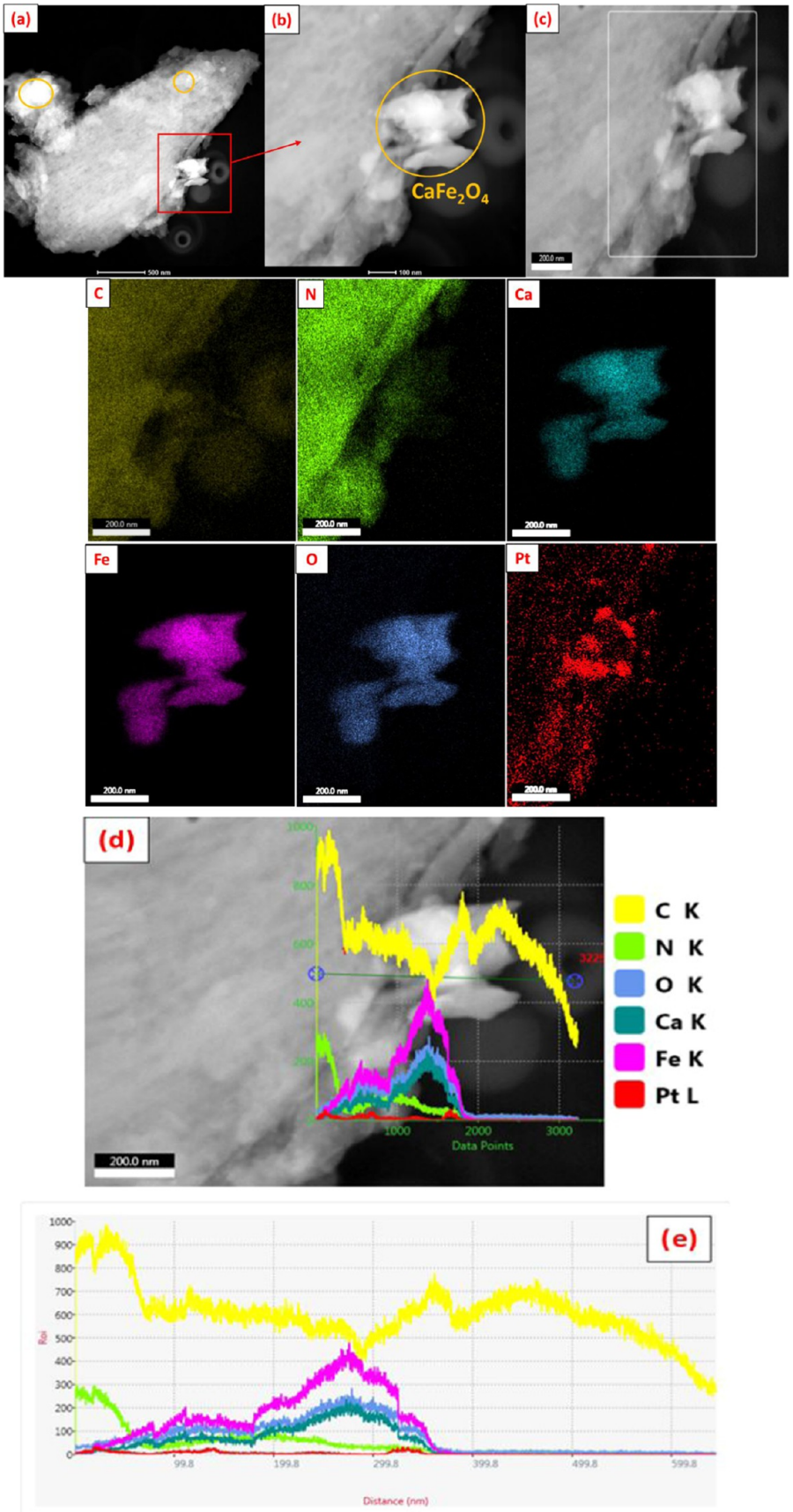

Figure 3. (a–c) HAADF-STEM images of Pt–CFO/NSCN, elemental mapping of C, N, Ca, Fe, and Pt over the selected rectangular area shown in (c), X-ray line mapping over the HAADF-STEM image (d), and the corresponding intensity pattern (e).

https://doi.org/10.1021/acsomega.4c06353
ACS Omega 2024, 9, 40182–40203

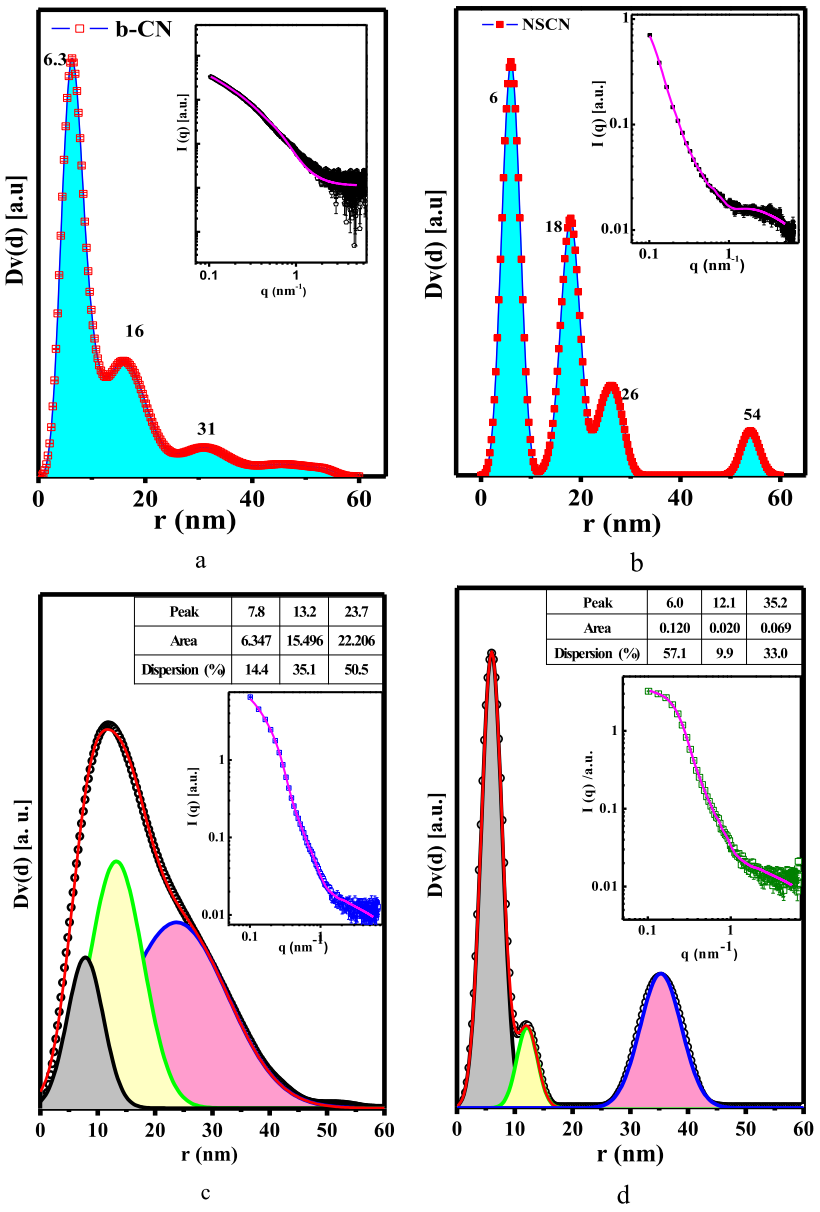

Figure 4. Pore radius distribution for (a) b-CN and (b) NSCN, and volume-weighted CFO particle size distribution in (c) CFO/b-CN and (d) CFO/NSCN extracted from the corresponding SAXS intensity pattern (background corrected data) given in the insets. The solid pink line inside the insets shows the model fit.

or less uniformly distributed over NSCN, whereas relatively large agglomerated irregularly shaped bright spots are due to CFO in HAADF-STEM images (Figure 3a−c). HAADF-STEM images confirmed the presence of individual C, N, Ca, Fe, O, and Pt elements in the Pt−CFO/NSCN photocatalyst. The energy dispersive X-ray spectrum (EDS or EDX) of the selected rectangular area sketched in the HAADF-STEM image (Figure 3c) was recorded, and the results are shown in subsequent intensity patterns (Figure 3d,e). The variation in the intensity of characteristic X-rays emitted from C ($K\alpha$ = 0.277 eV) and N ($K\alpha$ = 0.392 eV) of NSCN; Ca ($K\alpha$ = 3.690 eV), Fe ($K\alpha$ = 6.398 eV), and O ($K\alpha$ = 0.525 eV) of CFO; and Pt ($L\alpha$ = 9.441 eV) was monitored, mapping a line of 600 nm length, as shown in Figure 3(d,e). Carbon and N both showed a peak in the 0−80 nm region, and beyond that, both existed, but intensity declined. From 80 nm onward, the intensity of X-ray lines from Ca, Fe, and O increased steadily, and a peak was observed in the range of 200−350 nm. The profile of X-ray emission from Ca, Fe, and O was almost identical throughout 0−600 nm, revealing that the distribution of these elements represented the distribution of the $CaFe_2O_4$ phase in the sample. Thus, line mapping revealed that the CFO phase existed prominently in the region, nearly from 100 to 350 nm, with a peak at ∼260 nm. Pt nanoparticles have shown several peaks intermittently up to 350 nm, indicating the presence of Pt nanoparticles over both the NSCN and CFO phases. Both Pt and CFO were observed up to 350 nm, and beyond these, emissions only from carbon were observed. Our studies are in concurrence with Valdivel et al.,[40] in which agglomerated 100−200 nm-sized CFO particles were observed over CN. The morphological investigations in the present study have established that both CFO particles and Pt nanoparticles are immobilized over NSCN.

To further understand the microstructure of the photocatalysts, small-angle X-ray scattering (SAXS) measurements

https://doi.org/10.1021/acsomega.4c06353
ACS Omega 2024, 9, 40182−40203

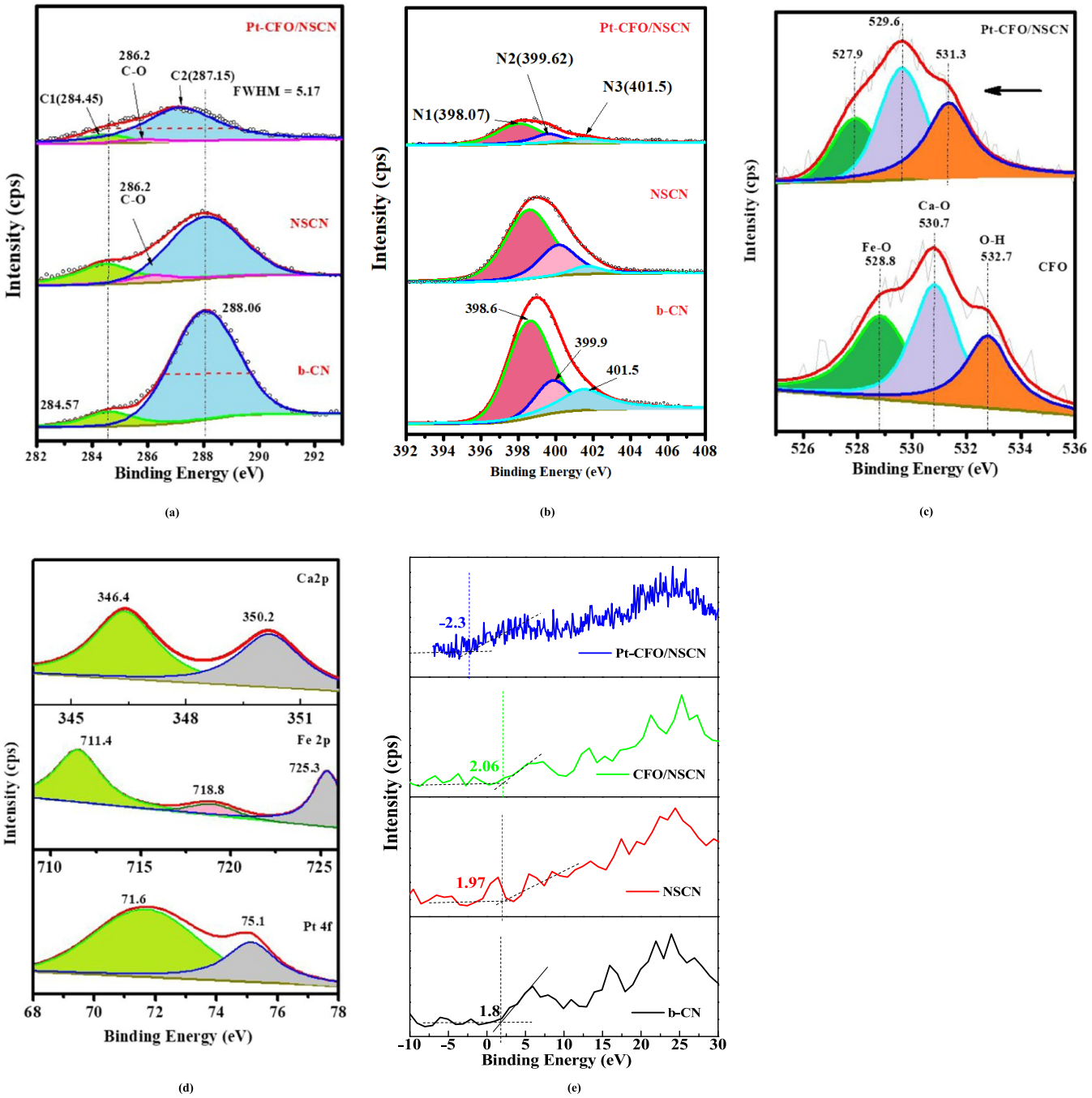

Figure 5. High-resolution XPS spectra of (a) C 1s, (b) N 1s, and (c) O 1s for different samples and (d) Ca 2p, Fe 2p, and Pt 4f in Pt−CFO/NSCN. (e) VBM- XPS spectra recorded for different samples.

were carried out. The pore size distribution is obtained by analyzing the SAXS data, assuming the presence of polydispersed spherical pores of radii in the range of 1−60 nm. The volume-weighted pore size distribution of b-CN and NSCN samples is given in Figure 4(a,b). The solid line inside inset shows the simulated scattering curve obtained for the pore size distribution. Pristine CN showed a majority of the pores in the microporous range centered at 6.3 nm and minor peaks at around 16 and 31 nm (Figure 4a). On exfoliation, the size and distribution of pores altered. Although the most intense peak or the maximum number of pores of 6 nm radii were retained, in addition, a few more peaks at higher radii of 18, 26, and 54 nm were observed (Figure 4b).

To obtain quantitative information about the particle size of different samples, SAXS was recorded in q ranging from 0.1 to 6 nm^{-1} and was analyzed using the polydisperse sphere model. In the case of a polydisperse population of spherical particles, the scattering pattern is derived as a sum of the scattering from individual size particles, $I_p(q, R)$, weighted by the distribution function, as given by the following equation

$$I(q, R) \propto \int_0^{R_{max}} D_v(R) R^3 I_p(q, R) dR$$

https://doi.org/10.1021/acsomega.4c06353
ACS Omega 2024, 9, 40182−40203

$$I_p(q, R) = K\Delta\rho^2 V_p\left(\frac{\sin(qR) - qR\cos(qR)}{(qR)^3}\right)2$$

where $D_v(R)$ is the volume-weighted particle size distribution, K is a constant subject to the instrument geometry, $\Delta\rho$ is the scattering contrast obtained by taking the difference in the electron densities of the matrix and particle, and V_p is the particle volume. Based on these equations, the particle size distribution (PSD) of CFO particles in CFO/b-CN and CFO/NSCN was derived from the SAXS pattern (inset of Figure 4c,d). PSD in curve c clearly indicated broad distribution for CFO/b-CN, in contrast to curve d, in which quite well-defined peaks were observed for CFO/NSCN. In both samples, particles in the range of 0−48 nm were formed. The broad band of CFO/b-CN was deconvoluted to extract three peaks at 7.8, 13.2, and 23.7 nm. The peak area under individual particle sizes is tabulated in the inset of Figure 4c,d for CFO/b-CN and CFO/NSCN, respectively. It revealed that the maximum number of CFO particles is of larger size, corresponding to 23.7 nm, as compared to 13.2 and 7.8 nm in CFO/b-CN (Figure 4c), while in CFO/NSCN (Figure 4d), well-resolved peaks corresponding to 6, 12.1, and 35.2 nm were observed and the majority of particles were of mean particle radii of 6 nm and few were in the range of 12−35.2 nm. The population of smaller particles is relatively higher in CFO/NSCN as compared to CFO/b-CN. As far as catalytic activity is concerned, it is the small-sized particles that are available on the surface and play an important role in the adsorption and photocatalytic reduction of water molecules. The particles with sizes >6−8 nm may remain in the agglomerated form and will not be available on the surface for catalysis. Relative dispersion (%) of dispersed-phase CFO on support b-CN or NSCN can be calculated by considering the ratio of the peak area of the peak corresponding to the smallest particles divided by the total peak area, as estimated in the table given in the insets of Figure 4c,d. Thus, 57% percent relative dispersion (6 nm) was obtained for CFO/NSCN as compared to 14.4% (7.8 nm) in CFO/b-CN (Table 2). It reveals that NSCN offers a large surface area and is a better host or support for uniform immobilization of CFO particles compared to b-CN. During exfoliation of bulk into nanosheets, porosity was induced, accompanied by a high surface area. Thus, NSCN forms superior contact with p-type spinel CFO, leading to efficient p−n nanoheterojunctions as compared to bulk-CN. Although TEM and HRTEM show that CFO particles are agglomerated, SAXS results confirm that NSCN has a superior morphology. 2D nanosheets of NSCN facilitate homogeneous and fine dispersion of CFO particles, typically of 6−8 nm size.

The above results are summarized as follows: (i) The few-layer morphology of NSCN showing well-resolved layers with 0.35 nm width was established over the multilayer morphology of bulk carbon nitride. (ii) Nanoparticles of Pt with 2−4 nm size were identified. (iii) Both Pt nps (hkl_{111}, hkl_{220}) and CFO particles (hkl_{214}, hkl_{113}) coexisted as confirmed by HRTEM/SAED and X-ray line mapping, thus establishing fabrication of Pt/CFO/NSCN heterojunctions. (iii) Superior morphology and particle size distribution were observed in CFO/NSCN as compared to CFO/b-CN from SAXS. (iv) NSCN is a better support, allowing 57% of total CFO particles to immobilize uniformly in small particles of 6 nm as compared to 14% relative dispersion offered by b-CN.

3.4. Oxide−Nitride Interactions. Survey scans of b-CN, NSCN, and Pt/NSCN/CFO are given in the Supporting Information (Figure S6), displaying peaks due to expected elements such as C, N, Ca, Fe, O, and Pt. The intensity of the O peak was significantly higher for NSCN than for b-CN (Figure S6a,b), indicating oxidation of b-CN during the treatment by highly oxidizing sulfuric acid in the exfoliation process. High-resolution C 1s spectra recorded for b-CN, NSCN, and Pt/CFO/NSCN are compared in Figure 5a. On deconvolution of the C 1s spectrum, two distinct peaks were observed in b-CN (Figure 5a), first at 284.57 (C1) due to graphitic carbon (C−[C, H]) or surface-adsorbed carbon and a second peak appears at 288.06 eV (C2), attributed to sp^2-hybridized carbon bonded to nitrogen (N−C═N) in the tri-s-triazine or heptazine rings of carbon nitride.[55] On exfoliation, an additional peak appeared at 286.2 eV attributed to C═O, as also reported by others.[41,56] This peak was not observed in b-CN. However, after acid-mediated exfoliation, oxidation of surface carbon is possible. Peaks due to C−O type interactions are evident in Pt−CFO/NSCN also (Figure 5a), possibly due to the interaction of the carbon of carbon nitride nanosheets with the oxygen of calcium ferrite.[41,56] The intensities of both C1 and C2 decreased notably in both NSCN and Pt/CFO/NSCN samples, as revealed from the deconvoluted graphs shown in Figure 5a. Since exfoliation resulted in a few-layer morphology, as shown by HRTEM, the contribution of both C1 and C2 is expected to decline in XPS. High-resolution N 1s spectra were deconvoluted into three peaks for b-CN, NSCN, and Pt/NSCN/CFO, as shown in Figure 5b. The peak centered at around 398.61 eV in b-CN is assigned to the sp^2-hybridized aromatic nitrogen (N1) bonded to carbon in the framework of the triazine unit (C═N−C), and the peak at 399.9 eV appears due to tertiary nitrogen (N2) in $N-(C)_3$, while the low-intensity peak at around 401.5 eV (N3) can be attributed to the amino functions carrying hydrogen (C−N−H), which is related to structural defects and incomplete condensation (Figure 5b).[57] On exfoliation, nanosheets showed a drastic fall in the intensity of N peaks and peaks appeared at 398.6, 400.2, and 401.7 eV for all three types N1, N2, and N3 respectively, which are slightly higher as compared to N in Pt−NSCN/CFO (398, 399.6, and 401.5 eV, respectively, in Figure 5b). A shift of binding energy to the lower side in the XPS spectra of both C 1s and N 1s was observed in the Pt/NSCN/CFO heterostructure as compared to parent NSCN. It signifies transfer of electrons induced by an internal electric field generated by fabrication of the p−n heterojunction at the CFO/NSCN interface.[56] This provides evidence that interfacial contact or p−n heterojunctions between CFO and NSCN are established during solvothermal synthesis of the CFO/NSCN composite. On exfoliation, the number of layers in the stack is limited, and a considerable decrease in the intensity of both C and N peaks was observed. However, the relative intensity of N3 increased as compared to N1 and N2 in Pt−CFO/NSCN. Thus, the contribution of N3 increased in total N in Pt−CFO/NSCN as compared to b-CN (Figure 5b). The ratio of N3 to total N (N1 + N2 + N3) was much higher for Pt−CFO/NSCN and NSCN as compared to b-CN. The unfolding of the polymeric sheets of b-CN into nanosheets is accompanied by an increased number of terminal amino groups and unsaturated N species on the surface, leading to an increased content of N3. The FWHM of the C 1s peak was ∼3 for b-CN and increased to 3.4 in exfoliated nanosheets and further increased considerably to 5.5 in Pt−CFO/NSCN. Band bending is evident by the peak shift or broadening of core levels. An increase in the FWHM of core levels (1s C or 1s N) signifies the increased band bending due to interactions of CFO with NSCN leading to the formation of p−

https://doi.org/10.1021/acsomega.4c06353
ACS Omega 2024, 9, 40182−40203

n heterojunctions.[58] The N/C ratio on the surface was calculated using XPS (Table 3) and was found to be 1.33 in b-CN and decreased to 1.06 in NSCN and 0.92 in Pt−CFO/NSCN, showing N deficit due to surface oxidation by H_2SO_4. Binding energies of all elements, along with surface elemental composition in different samples, are provided in Table 3.

The high-resolution O 1s XPS spectrum for pure phase CFO (Figure 5c) was deconvoluted into three peaks, namely, 528.8, 530.7, and 532.7 eV, attributed to the lattice oxygen Fe−O, Ca−O, and surface-adsorbed oxygen species, respectively.[59] Further, in the Pt−CFO/NSCN heterojunction, the deconvoluted O 1s peaks appeared at 527.9, 529.6, and 531.3 eV, which are shifted toward lower binding energy compared to parent CFO, as shown in Figure 5c. This shift in binding energy for the heterojunction can be explained on the basis of the strong interaction between NSCN and CFO. Zhang et al.[60] reported such results to originate from the decrease in electron concentration in NSCN and the increased electron concentration in CFO due to the strong interaction between them based upon interfacial charge transfer in heterojunctions.

The XPS spectra of Ca 2p, Fe 2p, and Pt 4f belonging to Pt−CFO/NSCN are shown in Figure 5d. Characteristic peaks due to Ca $2p_{3/2}$ and Ca $2p_{1/2}$ appear at 346.4 and 350.2 eV, respectively.[61] The high-resolution Fe 2p XPS spectrum (Figure 5d) consists of two peaks at 711.4 and 725.3 eV, corresponding to Fe $2p_{3/2}$ and Fe $2p_{1/2}$ spins, respectively, confirming the oxidation state of Fe to be +3 in CFO.[62] Typical satellite peaks at 718.8 eV due to Fe were also observed. The Pt 4f XPS spectrum (Figure 5d) was deconvoluted into two peaks at 71.6 and 75.1 eV, corresponding to Pt $4f_{7/2}$ and Pt $4f_{5/2}$, respectively.[63] The binding energy value of 71.69 eV for the Pt $4f_{7/2}$ state is a little higher than zero-valent metallic Pt but is significantly lower than Pt(II) and Pt(IV), which appear at 74.2 and 75.0 eV for PtO and PtO_2 species, respectively. This suggests that Pt exists in an electron-deficient state due to the interaction between the metal and support in Pt−CFO/NSCN. The partial positive charge on Pt is imparted due to bond formation between Pt and CN. The location and electronic state of such electron-deficient Pt sites formed during photodeposition favor hydrogen evolution reactions.[64]

The valence band maximum was estimated using valence band XPS, and the value was 1.80 eV for the parent carbon nitride (Figure 5e). After exfoliation, it increased to 1.97 eV, and after dispersion of CFO over NSCN, it further increased to 2.06 eV. The VBM-XPS profiles of NSCN and CFO/NSCN are similar to that of parent b-CN and almost overlap with it. However, Pt dispersion resulted in the VBM of −2.3 eV in Pt−CFO/NSCN, which is drastically different from that of parent b-CN.

Carbon nitride-based photocatalysts are normally excited in the range of 340−380 nm to yield photoluminescence emission (PL) spectra ranging from 400 to 600 nm with a peak at 453 nm (Figure 6a). The main photoluminescence band from 400 to 600 nm is composed of three transitions, namely, sp^3 C−N σ band, sp^2 C−N π band, and the LP state of the bridge nitride atom.[65] NSCN shows a blue shift in the luminescence peak to 436 nm, confirming a slight increase in the band gap on exfoliation. The interactions between carbon nitride and spinel CFO or the formation of functional heterojunctions at the interface of two different phases was evident by a decrease in PL intensity. The photogenerated electrons/holes generated at the edge of a semiconductor are channeled through these heterojunctions to the CB/VB, respectively, of the other

Table 3. Binding Energies and Surface Elemental Compositions Derived from the XPS of Different Samples

s. no.	sample	binding energy (eV)						chemical composition (atom %)						N/C (expected = 1.33)	Fe/Ca (expected = 2)
		C 1s	N 1s	O 1s	Ca 2p	Fe 2p	Pt 4f	C	N	Ca	Fe	O	Pt		
1	b-CN	284.57 (C1), 288.06 (C2)	398.6 (N1) 399.9 (N2) 401.5 (N3)					43.4	56.6					1.30	
2	NSCN	284.52 (C1) 286.2 (C−O) 288.06 (C2)	398.6 (N1) 400.2 (N2) 401.68 (N3)					48.4	51.6					1.06	
3	CFO			528.8 (Fe−O) 530.7 (Ca−O) 532.7 (O−H)	346.05 ($2p_{3/2}$) 349.66 ($2p_{1/2}$)	712.54 ($2p_{3/2}$) 724.82 ($2p_{1/2}$) 719.48				2.81	3.49	93.7			1.25
4	Pt−CFO/NSCN	284.45 (C1) 286.2 (C−O) 287.15 (C2)	398.07 (N1) 399.62 (N2) 401.5 (N3)	527.9 (Fe−O) 529.6 (Ca−O) 531.3 (O−H)	346.4 ($2p_{3/2}$) 350.2 ($2p_{1/2}$)	711.4 ($2p_{3/2}$) 725.3 ($2p_{1/2}$) 718.8	71.6 ($4f_{7/2}$) 75.1 ($4f_{5/2}$)	36.2	33.4	2.86	6.75	19.3	1.07	0.92	2.36

https://doi.org/10.1021/acsomega.4c06353
ACS Omega 2024, 9, 40182−40203

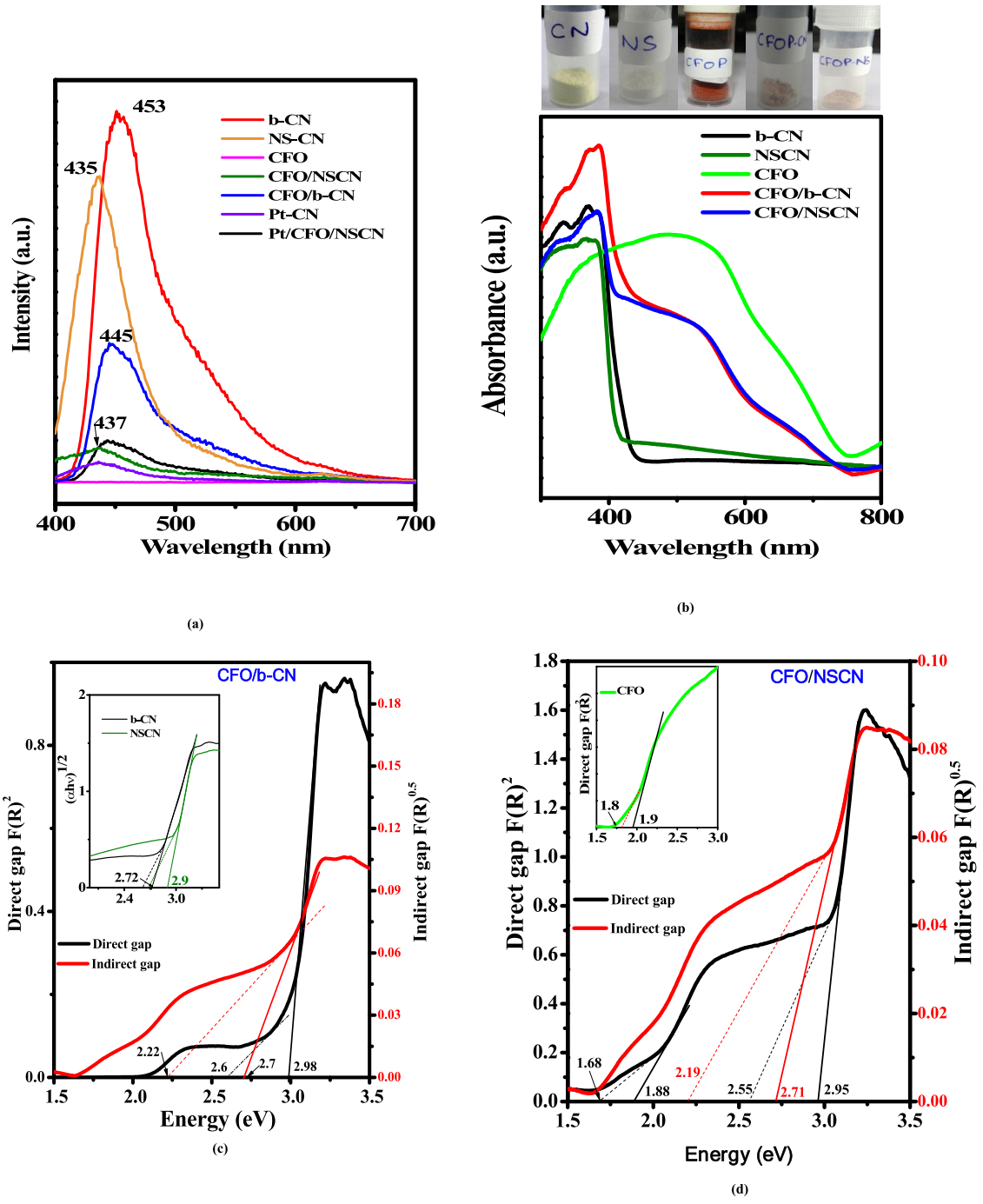

Figure 6. (a) Photoluminescence spectra of different samples excited at 350 nm, (b) UV−visible DRS spectra of all samples, (c, d) Kubelka−Munk transformed Tauc plots of CFO/b-CN and CFO/NSCN. Band gaps and sub-band gaps of b-CN, NSCN, and CFO are derived from Tauc plots shown in the insets of (c, d). Tauc plot of p−n heterojunctions CFO/b-CN and CFO/NSCN was prepared using both direct and indirect band gap equations.

contributing semiconductor and, this way, helps in charge (e^-/h^+) separation and suppression of the recombination reaction. The delayed or suppressed recombination is evident by the decrease in the intensity of the PL peak. The trend of PL intensity was b-CN > NSCN > 1 wt %CFO/b-CN > 1 wt % CFO/NSCN ∼ 1 wt %Pt−CFO/NSCN > 1 wt %Pt/b-CN. CFO-dispersed CN and NSCN samples have resulted in a significant decrease in photoluminescence intensity or suppression of recombination reactions as compared to pure parent compounds.

3.5. Optical and Electronic Properties and Band Structure. Optical properties or light absorption characteristics are very crucial for prospective semiconductors and are investigated by recording UV−visible DRS (Figure 6b). Parent yellowish bulk carbon nitride displayed an absorption edge at ∼450 nm, corresponding to an indirect band gap of ∼2.72 eV, in agreement with the reported studies.[34] On exfoliation, the color changed from yellow to whitish yellow due to a decrease in the number of layers in the 002 plane or decreased crystallinity, resulting in a blue shift of the absorption edge to 420 nm. The Tauc plot (inset of Figure 6c) demonstrated an increase in the

https://doi.org/10.1021/acsomega.4c06353
ACS Omega 2024, 9, 40182−40203

Table 4. Optical and Electronic Properties of Different Samples

sample	band gap from Tauc plot (eV)	sub-band gap (Urbach tailing) from Tauc plot (eV)	width of CB tail states	slope/type of semiconductor from M−S plot	V_{fb} Ag/AgCl at pH = 6.8	V_{fb} vs RHE pH = 0	CB_{min} (V vs RHE)[a]	VB_{max} (V vs RHE)[b]	charge carrier density (m^{-3})
b-CN	2.72	2.61	0.11	positive/n-type	−1.03	−0.4518	−0.5518	2.1682	3.99×10^{25}
NSCN	2.90	2.68	0.22	positive/n-type	−1.31	−0.7118	−0.81	2.09	4.56×10^{25}
CFO	1.90	1.80	0.10	negative/p-type	1.73	2.3282	0.52	2.4282	2.58×10^{22}
CFO/NSCN	2.71 (NSCN)	2.19 (NSCN)	0.52 (NSCN)	inverted V (p−n heterojunction)	−1.16 (NSCN)	−0.5618 (NSCN)	−0.66 (NSCN)	2.24 (NSCN)	5.0×10^{23} (NSCN)
	1.88 (CFO)	1.68 (CFO)	0.20 (CFO)		0.057 (CFO)	0.6552 (CFO)	−1.1448 (CFO)	0.7552 (CFO)	6.98×10^{21} (CFO)

[a]CB_{min} = conduction band minimum, close to V_{fb} for the n-type semiconductor. [b]VB_{max} = valence band maximum, close to V_{fb} for the p-type semiconductor

band gap on exfoliation from 2.72 eV (b-CN) to 2.9 eV (NSCN). However, pure phase spinel, CFO dark brick red color, is a low-band-gap semiconductor, and its DRS encompasses all wavelengths from 400 to 800 nm (Figure 6b). The Tauc plot of pure phase CFO was fitted into a direct band gap of 1.9 eV (inset of Figure 6d). To enhance the visible light absorption of carbon nitride, it was simply integrated with the low-band-gap CFO semiconductor into a composite material. Dispersion of 1 wt % CFO on CN significantly influenced the optical properties of CFO/b-CN and CFO/NSCN composites. Visual colors of both CFO/b-CN and CFO/NSCN transformed from yellow to beige (light brown), and accordingly, the absorption edge of carbon nitride (up to 450 nm) was fused with CFO (450−750 nm), as reflected in the DRS patterns shown in Figure 6b. The heterojunctions are formed between two dissimilar semiconductors, where CFO is a p-type and direct-band-gap semiconductor, while CN is an n-type and indirect-band-gap semiconductor. Thus, Tauc plots were fitted considering both direct and indirect band gap equations, as shown in Figure 6c,d. Accordingly, two absorption edges were observed in both CFO/b-CN and CFO/NSCN; one is at 2.7−2.9 eV (CN/NSCN) and the other is at a much lower band gap of ∼1.85−2.1 eV contributed by CFO. Tauc plots of CFO/b-CN and CFO/NSCN are shown in Figure 6c,d, respectively.

Along with the main absorption edge at ∼450 nm, a shoulder is also observed that extends up to 600 nm in the DRS of b-CN and is referred to as the Urbach tail.[34,66] It originates from the imperfections or intrinsic defects in the carbon nitride structure. Xue et al.[67] revealed that nitrogen vacancies play a crucial role in developing these intrinsic defects, which are manifested in the form of mid-gap states overlapping with the conduction band, also known as conduction band tail states. The difference in band gaps and sub-band gaps calculated using the main absorption edge and Urbach tail, respectively, helps in estimating the width of conduction band tail states or mid-gap states or shallow trap states.[34] The width of shallow trap states (STS) formed below the conduction band of parent compounds and in heterojunctions was also estimated from DRS. Tauc plots revealed band gap values of 2.72 and 2.9 eV and sub-band gaps of 2.61 and 2.68 eV for parent b-CN and NSCN, respectively, while a band gap of 2.7−2.9 and a sub-band gap of 2.19−2.55 eV are estimated at the carbon nitride edge for the CFO/NSCN composite considering both possibilities of fitting into direct and indirect band gap equations (Figure 6d and Table 4). Similarly, band gap and sub-band gap values of CFO/b-CN were estimated, as shown in Figure 6c and tabulated in Table 4. Designing heterojunctions between low-band-gap spinel CFO and relatively wide-band-gap b-CN or NSCN successfully improved the capability of carbon nitride to absorb visible light.

The M−S plot of $1/C^2$ versus applied voltage with respect to the Ag/AgCl electrode was recorded at 1 kHz (Figure 7) for the CFO/NSCN heterojunction and the individual control samples such as b-CN, NSCN, and pure phase of spinel $CaFe_2O_4$. Flat band potential (V_{FB}) was estimated using the following equation

$$\frac{1}{C^2} = \left(\frac{2}{q\varepsilon_0\varepsilon N_d A^2}\right)(V_{app} - V_{FB} - kT/q)$$

where ε is the dielectric constant of the semiconductor, ε_0 is the permittivity of vacuum, N_d is the donor density, V_{app} is the applied potential, V_{FB} is the flat band potential, and kT/q is the temperature-dependent term in the Mott−Schottky equation. The intercept of the linear plot at $1/C^2 = 0$ gives the flat band potential. Mott−Schottky plots of b-CN and NSCN photocatalyst (Figure 7a,b) samples have given a positive slope. Thus, confirming the n-type nature of the carbon nitride photocatalysts with electrons as the major carriers, while a negative slope for CFO confirmed its p-type semiconducting behavior with holes as major charge carriers (Figure 7c). Flat band potentials (V_{FB}) were estimated by extrapolating the linear region of the Mott−Schottky plots. It was found to be −1.05, −1.31, and +1.73 V with respect to Ag/AgCl for b-CN, NSCN, and CFO, respectively, as revealed in Figure 7 and tabulated in Table 4. The corresponding conduction band edge potentials and valence band edge potentials with respect to NHE (at pH 0) were also calculated, as listed in Table 4. The V_{FB} of NSCN was more negative than b-CN. It indicated that the flat band potential of b-CN shifted toward the cathodic side by −1.31 V with respect to Ag/AgCl after exfoliation. The increased charge carrier concentration in NSCN is responsible for shifting the Fermi level toward the conduction band or the cathodic side shift. The nature of the M−S plot shown in Figure 7d is a direct manifestation of p−n heterojunctions in CFO/NSCN. The Mott−Schottky plot of CFO/NSCN was inverted V type (Figure 7d), establishing the formation of p−n heterojunction and displaying two opposite slopes, one positive for NSCN and other negative in accordance with the p-type nature of CFO. The positive slope of the NSCN constituent was extrapolated, and V_{FB} was calculated to be −1.16 V (as compared to pure NSCN = −1.31 V), and the negative slope of "inverted V" belonged to the p-type CFO constituent with a V_{fb} of 0.057 V (pure CFO = 1.73 V) in the CFO/NSCN heterojunction (Figure 7d).

The slope of the Mott−Schottky plot $\left(\frac{2}{q\varepsilon_0\varepsilon N_d A^2}\right)$ has been employed to calculate charge carrier density (N_d) in different photocatalysts, as listed in Table 4. The maximum N_d of 4.56×10^{25} m^{-3} was observed for NSCN, while for b-CN and CFO,

https://doi.org/10.1021/acsomega.4c06353
ACS Omega 2024, 9, 40182−40203

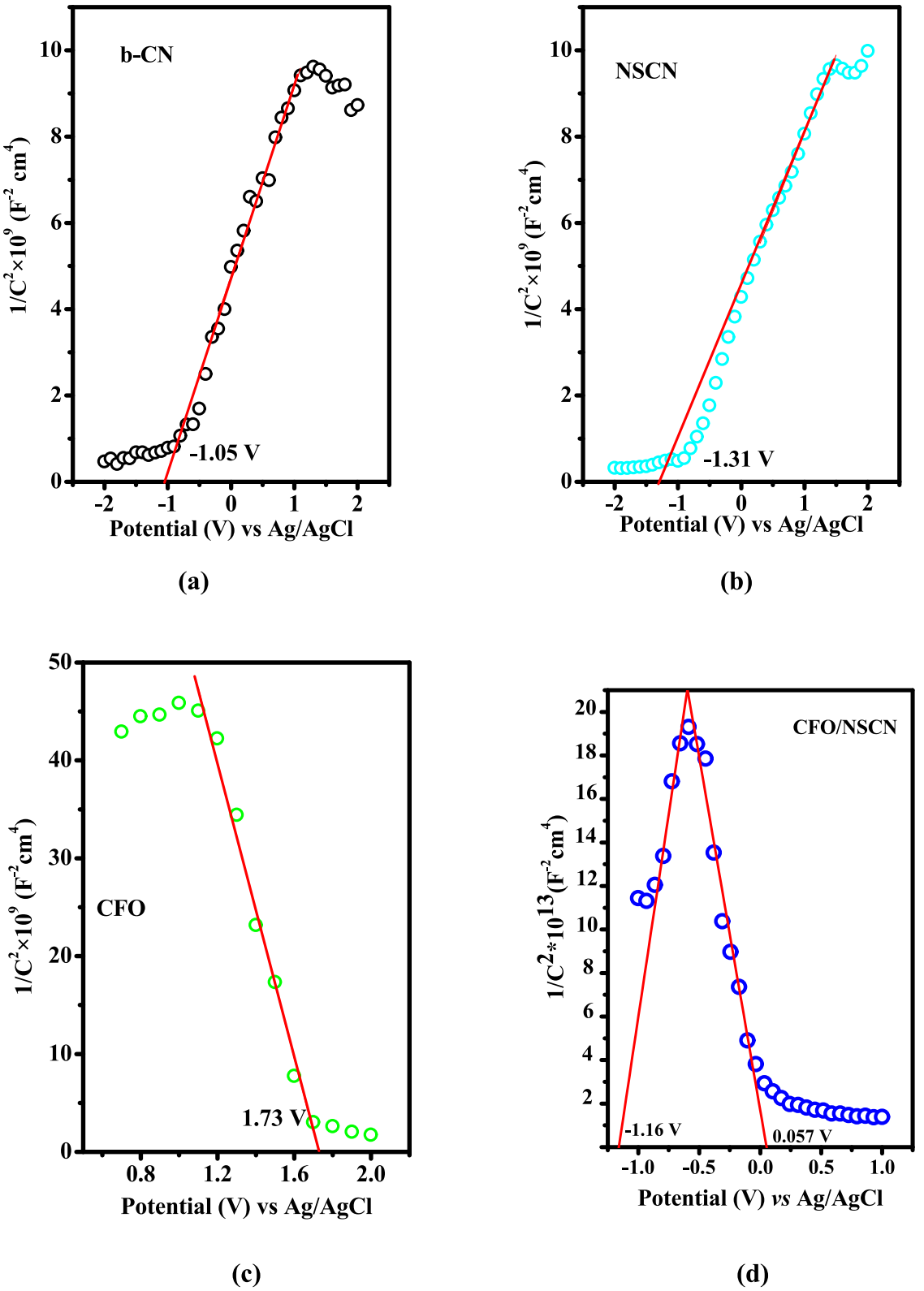

Figure 7. Mott−Schottky plots of (a) b-CN, (b) NSCN, (c) CFO, and (d) CFO/NSCN. An inverted V-shaped curve was obtained for p−n heterojunction (d). Flat band potential was measured using an intercept at the *x*-axis.

charge carrier densities were calculated to be 3.99×10^{25} and 2.58×10^{22} m^{-3}, respectively. The higher charge carrier density of NSCN compared to that of b-CN is one of the factors causing the enhanced rate of H_2 production in NSCN. At the same time, the slope of both p and n phases in the Mott−Schottky plot of the p−n heterostructure was found to be higher as compared to their pure counterparts (Table 4). Thus, the charge carrier density decreased on formation of p−n heterojunctions. This is in line with the fact that formation of a depletion layer takes

https://doi.org/10.1021/acsomega.4c06353
ACS Omega 2024, 9, 40182−40203

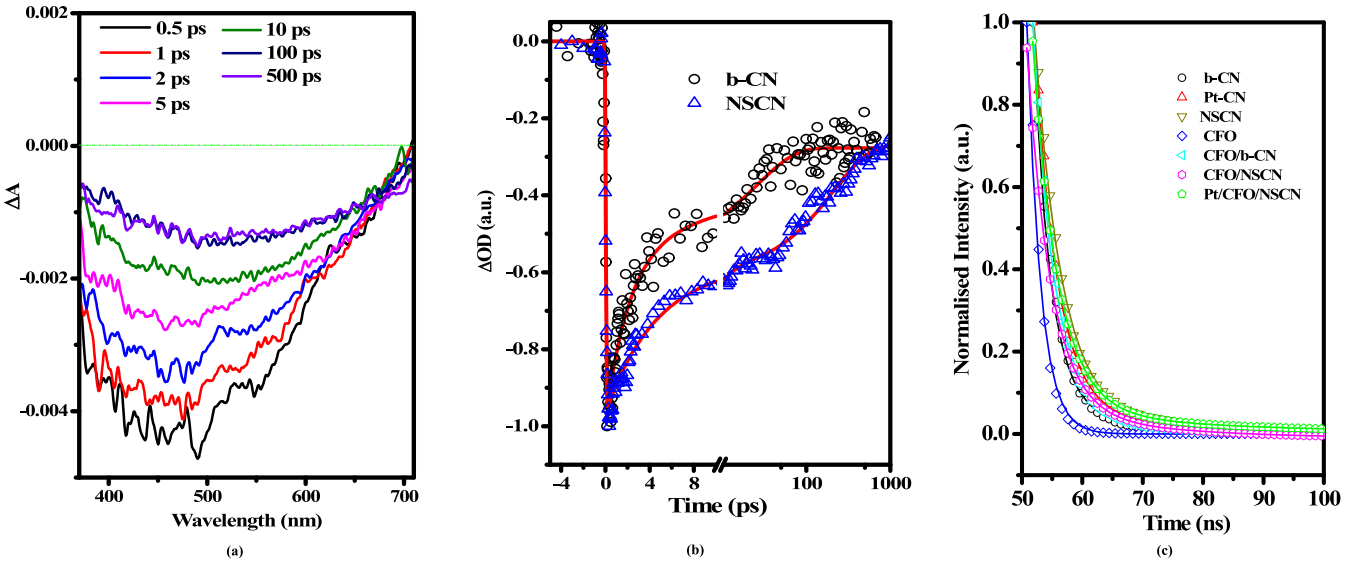

Figure 8. (a) Femtosecond transient absorption spectra (FsTAS) recorded at different time delays after excitation of b-CN at λ = 350 nm. (b) Kinetic traces of stimulated emission of b-CN (λ = 500 nm) and NSCN (λ = 550 nm). (c) Time-resolved photoluminescence (TRPL) spectra recorded of different photocatalysts on excitation at λ = 340 nm.

Table 5. Kinetic Parameters Derived from the FsTAS Decay Profile Recorded for b-CN and NSCN Samples (Figure 8b) and Fitted in the Triexponential Equation[a]

samples	τ_1 (ps)	A_1 (%)	k_1 (10^{11} s^{-1})[d]	τ_2 (ps)	A_2 (%)	k_2 (10^{10} s^{-1})	τ_3[c] (ps)	A_3 (%)	τ_{avg} (ps)[b]	k_{avg} (10^8 s^{-1})
NSCN (550 nm)	3.19	42	3.13	187	31	0.53	>1000	27	1881.8	5.31
b-CN (500 nm)	2.2	49	4.54	30	22	3.33	>1000	29	1306.8	7.65

[a]Triexponential equation is as follows $I(t) = A_1 \exp^{-t/\tau_1} + A_2 \exp^{-t/\tau_2} + A_3 \exp^{-t/\tau_3} + A_0$. [b]$\tau_{avg}$ (average lifetime) was calculated using the formula $\tau_{avg} = \frac{\sum A_i \tau_i}{\sum A_i}$. [c]$\tau_3$ values required to calculate τ_{avg} were taken from TRPL data given in Table 6. [d]Rate constant K was calculated by $k_i = \frac{1}{\tau_i}$.

place in the case of the p−n heterojunction, leading to lower charge carrier densities of both p- and n-type carriers.

3.6. Charge Transfer Kinetics. The pump−probe dynamics of bulk carbon nitride (b-CN) and nanosheet carbon nitride (NSCN) were studied by femtosecond transient absorption spectroscopy (FsTAS). Samples were dispersed in n-propanol and excited using a 350 nm femtosecond laser pulse and probed in the visible region by femtosecond white light continuum. Figures 8a and S7 show transient absorption spectra recorded at different time delays ranging from 0.5 to 500 ps (0.5, 1, 2, 10, 50, 100, 500 ps) for b-CN and NSCN, respectively. Both samples show a broad negative ground-state bleach signal in the 400−700 nm region, which originates from stimulated emission from the band gap transition as well as trap state recombination.[68,69] Steady-state emission of b-CN and NSCN samples dominantly appeared at 400−500 nm, which contributed to stimulated emission in the pump−probe experiment in this wavelength range. Stimulated emission (SE) in the 500−700 nm region observed in transient data possibly originates from the low-energy defect state. This SE signal from the defect state evolves very fast in the 0−200 ps time scale, while SE and the ground-state bleach signal in the 400−500 nm region decay slowly, and the majority of the signal persists for greater than 1 ns. Transient absorption kinetic traces of b-CN and NSCN are shown in Figure 8b. Triexponential fitting was performed to get three lifetimes τ_1, τ_2, and τ_3 along with their individual contributions A_1, A_2, and A_3, respectively, as listed in Table 5. The decay kinetic trace at 500 nm for b-CN (Figure 8b) revealed two short-lived components 2.2 (49%) and 30 ps (22%), and one long-lived component >1000 ps. The long-lived component was estimated using TRPL as given below. It has been reported earlier that the decay of photoexcited electrons is not a direct mechanism but takes place via trapping.[70,71] The short-lived components (τ_1 and τ_2) can be attributed to the trapping of photogenerated electrons in shallow traps. Photoexcited electrons are also trapped in deep trap states lying below H^+/H_2 reduction potential, which imparts a longer lifetime and is denoted by τ_3. From Table 5, both short-lived, τ_1 and τ_2, and long-lived, τ_3, lifetimes are longer in NSCN as compared to b-CN. Photoexcited electrons decay in 2.2 ps (τ_1, 49%) and 30 ps (τ_2, 22%) in bulk, which live much longer up to 3.19 (τ_1, 42%) and 187 ps (τ_2, 31%) on exfoliation into nanosheets, NSCN. τ_{avg} was estimated to be higher for NSCN (1881.8 ps) as compared to b-CN (1306.8 ps), which also includes long-lived τ_3 components. The recombination rate ($k_{avg} = 1/\tau_{avg}$) of photogenerated charge carriers in NSCN was calculated to be 5.31×10^8 s^{-1} compared to 7.65×10^8 s^{-1} in b-CN (Table 5), which also includes deep trapping and shows a 1.44-fold decrease in the rate of e^-/h^+ recombination in NSCN as compared to bulk b-CN. Deep trapping is detrimental to photocatalytic hydrogen yield and cannot be accurately calculated by FsTAS, as it takes place in nanoseconds (τ_3 > 1 ns). Exfoliation has induced defects, which has considerably improved the lifetimes of photogenerated charge carriers via shallow trap states (τ_2 of 187 ps) as compared to b-CN (τ_2 = 30 ps). Decay of photogenerated electrons via shallow trap states is delayed in NSCN ($\tau 2$ = 187 ps) as compared to b-CN (τ_2 = 30 ps), resulting in suppression of the rate of recombination by nearly six times in NSCN ($k = 0.53 \times 10^{10}$ s^{-1}) with respect to b-CN ($k = 3.33 \times 10^{10}$ s^{-1}). Lifetimes of charge carriers in CFO-

https://doi.org/10.1021/acsomega.4c06353
ACS Omega 2024, 9, 40182−40203

dispersed samples, namely, CFO/b-CN and CFO/NSCN, could not be monitored by FsTAS due to strong fluorescence from CFO, which interfered with the analysis.

In order to get insights into the lifetime of long-lived (>1 ns) charge carriers, time-resolved photoluminescence spectra were recorded at an excitation wavelength of 340 nm, as shown in Figure 8c. The obtained data were fitted using biexponential decay equations. It gives two lifetime values, τ_1 and τ_2, with corresponding amplitudes, A_1 and A_2, respectively, and the fitting parameter (R^2), as tabulated in Table 6. A lifetime of 4.48 ns was observed in b-CN, which increased to 6.75 ns in NSCN. This can be attributed to a decrease in the number of layers on exfoliation making transfer of e^-/h^+ to surface sites much faster, thus decreasing their recombination probability and/or electronic band structure changes induced by the quantum confinement effect in the nanosheets.[72] CFO has a low average lifetime of 2.34 ns for photogenerated charge carriers, which is typical of low-band-gap spinel ferrite materials.[73] After the dispersion of CFO over b-CN and NSCN, the obtained nanoheterojunction materials CFO/b-CN and CFO/NSCN have average lifetimes of charge carriers of 4.88 and 9.49 ns, respectively. The obtained lifetime values are higher as compared to the parents due to the formation of the p−n heterojunction between p-type CFO and n-type carbon nitride, facilitating the separation of photogenerated e^-/h^+ pairs at the interface. NSCN is a relatively much better support for CFO dispersion as compared to b-CN. NSCN proved to suppress the rate of recombination drastically and offered much faster charge transfer kinetics as compared to b-CN for p−n heterojunctions. Pt−CFO/NSCN has a maximum lifetime of photogenerated charge carriers, i.e., 10.03 ns. Efficient separation of charge carriers in Pt−CFO/NSCN is attributed to the combined effect of Schottky junctions created by Pt nanoparticles on the surface, driving fast transfer of electrons from bulk to the surface and indeed p−n heterojunctions, which efficiently separate photogenerated electrons toward n-type and holes toward p-type CFO at the interface during photocatalytic reactions.

Table 6. Lifetimes of Photogenerated e^-/h^+ Pairs Obtained from Time-Resolved Photoluminescence (TRPL) Spectra Given in Figure 8c

sample	τ_1 (ns)	A_1 (%)	τ_2 (ns)	A_2 (%)	τ_{avg} (ns)[a]	R^2
b-CN	2.54	61.0	7.55	39.0	4.48	0.998
NSCN	4.59	85.3	19.34	14.7	6.75	0.998
CFO	2.34	100			2.34	0.993
CFO/b-CN	3.09	60.0	7.56	40.0	4.88	0.997
CFO/NSCN	4.10	70.7	22.52	29.3	9.49	0.963
Pt−CFO/NSCN	4.20	72.3	25.26	27.7	10.03	0.998

[a]Average lifetime: $\tau_{avg} = \frac{\sum A_i \tau_i^2}{\sum A_i \tau_i}$.

3.7. Modeling of H_2O/H_3O^+ Adsorption over Different Photocatalysts Using Molecular Dynamics. Figure 9 displays snapshots of the final conformations equivalent to NSCN, CFO/NSCN, Pt−NSCN, and Pt−CFO/NSCN photocatalytic systems. The calculations involved in the construction of these conformations/model systems and other details are given in Supporting Information (S4 and Figures S8 and S9). The snapshots provide a comparison of the adsorption capability of H_3O^+ ions on the surface of different photocatalytic formulations. It improved in the order NSCN < Pt−NSCN < CFO/NSCN < Pt−CFO/NSCN. Thus, the Pt−CFO/NSCN system has the best adsorption capacity for H_3O^+. Here, snapshots taken are capturing a single conformation of the system at a given time. In fact, in equilibrium, a system can exist or form a large number of conformations; thus, a time-average picture is crucial to represent a system more accurately.[74]

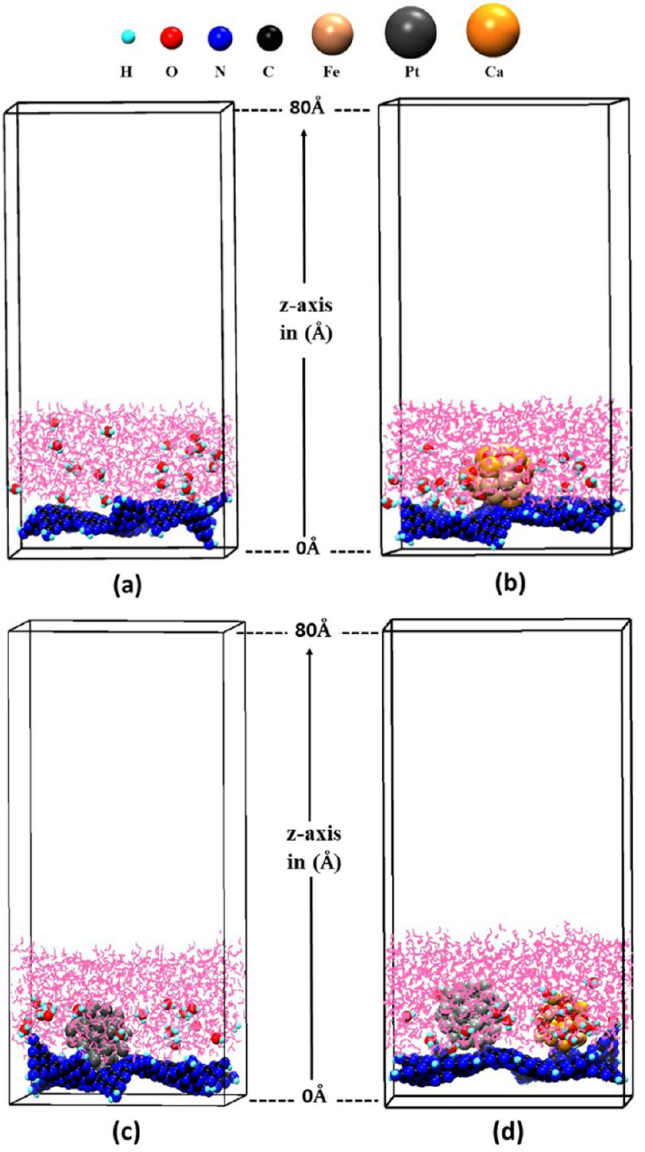

Figure 9. Snapshots of (a) NSCN, (b) CFO/NSCN, (c) Pt−NSCN, and (d) Pt−CFO/NSCN systems at the end of the simulation run. Water molecules in these models are given in pink for better visibility.

Density profiles are shown in Figure S10, in which the molecular density of H_3O^+ ions (molecules/[Å^3]) is plotted against the distance along the *z*-axis of the simulation box (in Å) corresponding to the above photocatalytic systems. These density profiles are time averages of the last two nanosecond production runs. The blue graph in each plot depicts the change in H_3O^+ ion density with the distance along the *z*-axis of the rectangular simulation box. In all graphs, the small red peak depicts the location of NSCN. The pink peak represents the location of the CFO cluster in curves b and d and black represents the Pt cluster in curves c and d. Figure S10a shows no blue peak adjacent to the red peak, indicating poor H_3O^+ ion adsorption on NSCN. Figure S10b displays a prominent blue peak surrounding the pink (CFO) peak. Thus, H_3O^+ ions

https://doi.org/10.1021/acsomega.4c06353
ACS Omega 2024, 9, 40182−40203

surround the CFO cluster, increasing the overall rate of H_3O^+ ion adsorption to the catalyst surface. The H_3O^+ ion adsorption effect of the Pt cluster is less than that due to the CFO cluster, as shown in Figure S10c, while in curve d of Figure S10, there are two prominent blue peaks surrounding both CFO (pink) and Pt (black) clusters. Thus, density profiles also support the fact that the adsorption of H_3O^+ ions is maximum for the sample corresponding to the Pt−CFO/NSCN composite system. Pt/NSCN allows weak interactions between Pt and H_3O^+; however, in the presence of CFO, the adsorption capability of Pt−CFO/NSCN is enhanced considerably.

A radial distribution function (RDF) plot based on the d-model reveals the probability of the occurrence of an atom type near another atom type. RDF plots between different atoms of the Pt−CFO/NSCN composite with H_3O^+ and H_2O molecules are shown in Figure 10a,b, respectively. The intensity and the distance at which the first peak appears in each graph are crucial. The location and the intensity of the first peak of an RDF give the strength of interaction between the considered atom types. The first peak at ∼2.3 Å of the red plot has the highest intensity among all plots in Figure 10a. It shows a strong electrostatic interaction between the calcium atom of the CFO cluster and the O atom of H_3O^+ ions. The magenta peak (Figure 10a) represents the interaction between the ring nitrogen of the NSCN part and the hydrogen of the H_3O^+ ions. Its first peak at ∼2.2 Å is of low intensity, signifying weak interaction. The H_3O^+ ion interacts with the nitrogen of the heptazine rings of NSCN through the hydrogen bond.[75] Furthermore, a very weak peak appears at an ∼2.4 Å distance due to the interaction of the platinum atom of the Pt cluster with the oxygen atom of H_3O^+ ions in the black curve. The peak at ∼2.5 Å appeared during the interaction of the carbon of the heptazine rings of NSCN with the oxygen of H_3O^+ ions, as observed in the blue plot.

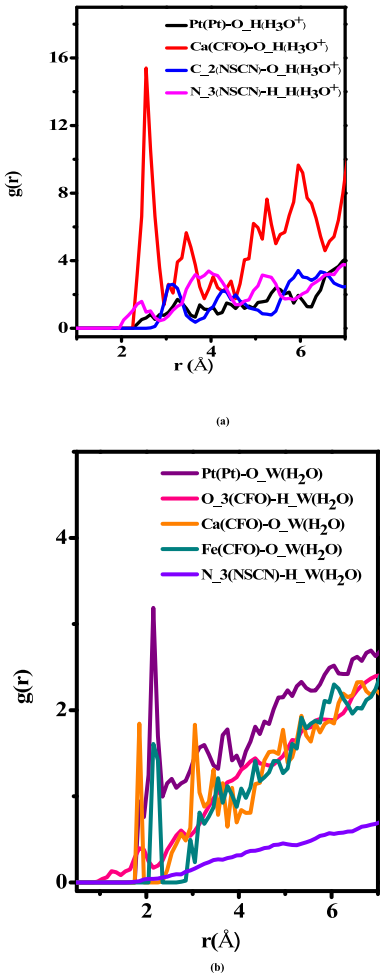

Figure 10. Radial distribution function (RDF) plot for the interaction between different atoms of the Pt−CFO/NSCN system with atoms of (a) H_3O^+ and (b) water. (Abbreviations: N_3—ring nitrogen of the NSCN part, C_2—ring carbon of the NSCN part, Ca—calcium atom of the CFO part, Fe—iron atom of the CFO part, O_3—oxygen atom of the CFO part, Pt—platinum atom of the Pt43 part, O_W—oxygen atom of water, H_W—hydrogen atom of water, O_H—oxygen atom of the H_3O^+ ion, H_H—hydrogen atom of the H_3O^+ ion).

Figure 10b shows the interaction between the various atom types existing in the Pt−CFO/NSCN composite with water molecules. At ∼1.6 Å, the first peak of the pink plot depicts the interaction between an oxygen of the CFO cluster with the hydrogen atom of a water molecule. This peak indicates a hydrogen bonding interaction between these two atom types.[75] The first peaks of the orange and purple plots occur almost at the same distance, ∼1.8 Å. However, the intensity of the first peak of the orange plot is considerably higher. The orange plot depicts the interaction between the Ca of the CFO cluster with the O of H_2O molecules. The purple peak represents a strong interaction between a Pt atom (Pt cluster) and water's oxygen. Note that the purple graph also has a very intense second peak at ∼2.1 Å. No significant peaks for interactions between the NSCN and H_2O atom types are observed. From the above data, it is clear that prominent interactions are hydrogen bonding and electrostatic attraction between oppositely charged atoms. Also, interactions of both Ca and O in CFO are depicted with water molecules. Strong electrostatic interaction between oppositely charged Ca^{2+} ions of CFO and O^{2-} ions of H_2O is mainly responsible for enhanced adsorption capability exhibited by CFO toward water molecules.

Thus, it was observed that the CFO cluster adsorbs H_3O^+ ions very strongly through the electrostatic interaction between calcium and oxygen (of H_3O^+). The CFO cluster also strongly adsorbs H_2O molecules through two types of interactions. The adsorption of H_3O^+ ions on the NSCN sheet is primarily through hydrogen bond interaction with the ring nitrogen of the latter. Nevertheless, the NSCN sheet has a relatively poor affinity for water molecules. The interaction of the H_3O^+ ions with the Pt cluster is relatively weak. However, the Pt cluster displays a strong affinity for H_2O molecules. Water is the carrier for the H_3O^+ ions. Therefore, the affinity for water is a primary requirement for H_3O^+ ion adsorption. The CFO and Pt clusters' strong water affinity improves the H_3O^+ ion access to the NSCN sheet.

4. DISCUSSION

To date, several studies have investigated and emphasized the role of heterojunctions prepared by using spinel ferrites (MFe_2O_4, M = Ca, Zn, Co, Mn, Fe, Ni, etc.) with g-C_3N_4 in the enhancement of photocatalytic properties. Among these, very few reports, to the best of our knowledge, have evaluated $CaFe_2O_4$/CN composites for photocatalytic hydrogen generation from water. $CaFe_2O_4$ being a low-band-gap, magnetic ferrite has been reported as an efficient photocatalyst for water remediation involving degradation of dyes and other water contaminants.[40−47] The photocatalytic properties of selected ferrites/g-C_3N_4 heterojunctions along with other important features reported in the literature are summarized in Table S3.

https://doi.org/10.1021/acsomega.4c06353
ACS Omega 2024, 9, 40182−40203

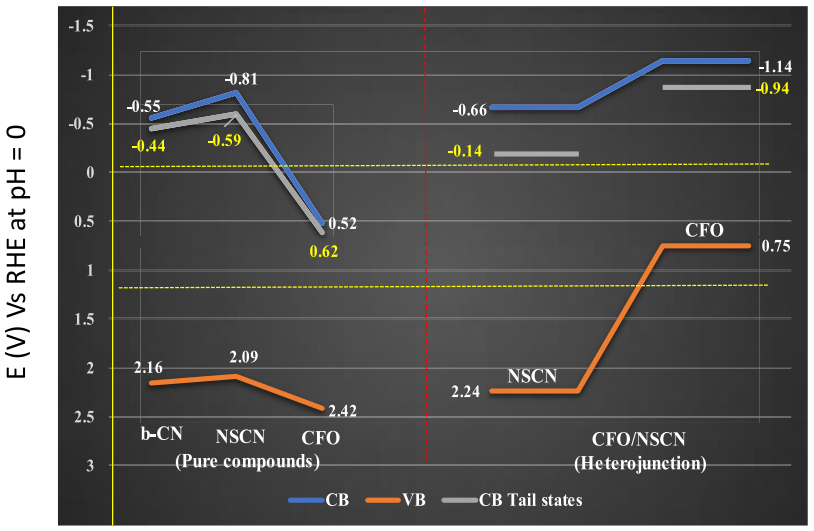

Figure 11. Band edge potentials of pure compounds b-CN, NSCN, and CFO (before contact) were estimated by M−S plots and compared with band edge potentials of a p−n heterojunction formed between CFO/NSCN after contact. Valence band (VB), conduction band (CB), and CB tail states/Urbach tail potentials (yellow font) for all samples are given. The potential required for reduction of pure water ($2H^+/H_2$ = 0 V, $H_2O/0.5\ O_2$ = 1.23 V) and oxidation versus RHE at pH = 0 are represented by yellow dotted lines for comparison.

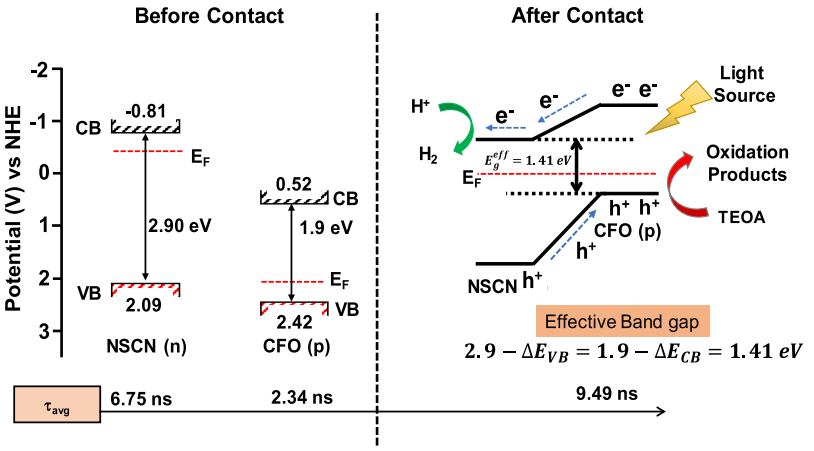

Figure 12. Schematic of the band diagram of pure phases CFO and NSCN compared with the type-II p−n heterojunction attained by CFO/NSCN as a result of Fermi level (E_f) equilibration is illustrated. The most probable mechanism of the photocatalytic reaction is proposed based on predictable transfer and separation of electrons and holes at the interface of the p−n CFO/NSCN heterojunction under light illumination. VBO and CBO were also estimated, and an effective band gap of 1.41 eV is achieved. Lifetimes of photogenerated charge carriers derived from TRPL support the photocatalytic mechanism.

Liu et al.[42] reported enhanced HER yield over these $CaFe_2O_4$/g-C_3N_4/CNT heterojunctions. Many studies[40,76,77] have used the Mulliken electronegativity theory for estimating the CB and VB values of CFO and g-C_3N_4. However, in the present study, CB and VB values were calculated experimentally using M−S plots and VBM-XPS of individual parent samples such as bulk-CN and nanosheets NSCN and CFO and were compared with the CB and VB of the heterojunction formed between NSCN and CFO after the contact. Based on the M−S plots, the CB and VB edge potentials of parent NSCN are determined to be −0.81 and 2.09 eV, respectively, while those of CFO were 0.52 eV (CB) and 2.42 eV (VB), respectively. The energy band structure diagram of parent compounds NSCN, CFO, and b-CN before contact is schematically illustrated in Figure 11.

When p-type CFO is brought in contact with the n-type NSCN, since the CB potential of NSCN is more negative than that of CFO, the electrons will flow from NSCN to CFO, resulting in the accumulation of negative charges in CFO close to the junction. Simultaneously, the holes will transfer from the more positive VB edge of CFO to the less positive VB edge of NSCN until the Fermi level equilibrates. Once the Fermi levels of CFO and NSCN equilibrate, further diffusion of electrons and holes will halt. Meanwhile, the energy bands of CFO shifted upward along with its Fermi level (E_F), and those of the NSCN shifted downward along with its Fermi level (E_F), as illustrated in Figure 11. After contact, in the heterojunction, CB and VB edges corresponding to the NSCN semiconductor were −0.66 and 2.24 eV, respectively, and for CFO, the CB edge was at −1.14 eV, and the VB edge was at 0.75 eV. Consequently, the lowest unoccupied molecular orbital (LUMO) of the CB of CFO is at a higher level than that of NSCN. Under visible light, both the semiconductors CFO and NSCN absorb photons of energy greater than their band gap energy. The electrons in the CB of p-type CFO are transferred to n-type NSCN, while holes moved from the VB of NSCN to the VB of CFO, thus leading to efficient charge separation at the heterojunctions. Thus, p−n

https://doi.org/10.1021/acsomega.4c06353
ACS Omega 2024, 9, 40182−40203

heterojunctions accelerate the charge separation and charge transfer kinetics, which is also evident by a decrease in intensity in PL and an increase in the lifetime of charge carriers in TRPL. A complete band alignment diagram at the interface of the CFO/NSCN heterojunction, including valence band offset (VBO) and conduction band offset (CBO), and time scales derived from TRPL and FsTAS are shown in Figure 12. It reveals that the effective band gap at the heterojunction is decreased to 1.41 eV, which is lower than the band gaps of individual semiconductors.

For understanding the functionality of p−n heterojunctions, few insights are very important. One is the nature of interactions or contact between two semiconductors, the second is the band alignment at the interface (as explained above), and the third is the charge transfer kinetics. The nature of interactions is critical for designing interfaces or interfacial engineering. The amount or molar ratio of the two semiconductors taken in the study is elementary for interfacial engineering. Here, in the present study, 1 wt % CFO is dispersed in both CFO/b-CN and CFO/NSCN. A CFO lean composition relative to g-C_3N_4 in CFO/b-CN will facilitate smooth unagglomerated and unhindered arrest of CFO molecules over g-C_3N_4 support, will also provide liberty to Pt atoms for free dispersion, and lastly will improve the accessibility for water molecules. The ratio of CFO to g-C_3N_4 is crucial for inducing close, superior contact with g-C_3N_4 layers/2D sheets as well as with Pt nanoparticles. Moreover, a higher concentration of CFO on the surface may block the penetration of light inside the layered structure. A superior morphology is observed here for CFO/CN molecules. Fine dispersion of CFO particles was observed over NSCN, as revealed by SAXS data. 57% dispersion of 6 nm-sized CFO on NSCN was observed, while b-CN supported 14% dispersion of 7.8 nm-sized CFO particles. 2−4 nm-sized Pt nanoparticles were observed in the 1 wt %Pt/1 wt % CFO/NSCN sample. Vadivel et al.[40] reported dispersion of 20−40 wt % CFO on b-CN and observed agglomeration in CFO particles. In another recent study, Shenoy et al.[41] mixed varying amounts of CFO (10−100 mg of as-synthesized CFO) with 10 g of urea before calcination at 550 °C for 2 h and observed a quasi-polymeric nature of the CFO/g-CN composite.

Among NSCN and b-CN, evidently, NSCN is a better support for CFO. HRTEM established that exfoliation of b-CN into nanosheets (NSCN) resulted in a few-layer morphology with 0.35 nm width. FsTAS verified suppression of recombination of photogenerated charge carriers by ∼6 times in NSCN (K_2 = 0.53 × 10^{10} s^{-1}) than b-CN (3.33 × 10^{10} s^{-1}; Table 5). Slower decay or enhanced lifetime of photogenerated charge carriers in a two-dimensional NSCN sample is mainly due to shallow traps. Exfoliation has induced defects, which has drastically improved the lifetimes of photogenerated charge carriers in shallow trap states (τ_2 of 187 ps) as compared to b-CN (τ_2 = 30 ps, Table 5). This contributed to the higher photocatalytic efficiency of NSCN over b-CN and CFO/NSCN over CFO/b-CN. Thus, it is essential to probe and understand the various photoexcitation processes going through inside, and it helps to design new and improved photocatalytic materials.

SAXS data indisputably established the higher porosity of nanosheets and a much better support for CFO as compared to b-CN. Interactions of CFO with NSCN through oxygen linkages were indicated by XPS. The present study establishes the superior morphology of NSCN to that of b-CN, resulting in stronger interactions with CFO. NSCN is superior to b-CN and forms effective p−n heterojunctions with CFO as compared to b-CN. Band bending was induced on formation of heterojunctions and was manifested by an increase in the fwhm of C 1s and N 1s XPS spectra of the Pt−CFO/NSCN composite as compared to parent compounds. Also, the width of shallow trap states of pure CFO (0.1 eV) and NSCN (0.22 eV) increased to 0.2 and 0.52 eV, respectively, when forming a contact in CFO/NSCN, as shown in Figure 11 and listed in Table 4. The additional shallow trap states are new channels for the transfer of photogenerated electrons from CFO to NSCN. VBM-XPS and Mott−Schottky plots helped in understanding and calculating the band alignment at the interface of CFO and NSCN. Increasing order of the average lifetime of charge carriers as deduced by TRPL was found to be CFO (2.34 ns) < b-CN (4.5 ns) < CFO/b-CN (4.88 ns) < NSCN (6.7 ns) < CFO/NSCN (9.5 ns) < Pt−CFO/NSCN (10.03 ns). TRPL studies confirmed the efficient charge separation by p−n heterojunctions formed using NSCN and CFO in the presence of Pt nanoparticles.

The role of CFO is not limited to enhancing light absorption capability and suppression of recombination reactions only. In addition, CFO dispersion on carbon nitride has also affected a very crucial aspect of heterogeneous catalysis, i.e., the adsorption of water molecules. Theoretical calculations by molecular dynamics (MD) have revealed that the adsorption capability of the carbon nitride-based photocatalyst for H_2O and H_3O^+ molecules is markedly improved by incorporation of CFO. The main results obtained from these MD calculations are that although NSCN does not have any preference or affinity toward either water or H_3O^+ ions, the presence of Ca^{2+} ions in the CFO cluster draws water molecules toward itself through electrostatic interactions. Moreover, Pt nanoparticles also showed enhanced attraction toward neutral water molecules. However, the affinity of Pt for charged H_3O^+ ions was poor. Thus, the presence of both CFO and Pt was beneficial for increasing the adsorption capability of Pt−CFO/NSCN. Pt allowed more and more water adsorption and probably facilitated the contact and access of water molecules with CFO in the Pt−CFO/NSCN photocatalytic system. The presence of CFO further enhanced the adsorption, as its electrostatic attractive forces retained H_3O^+ ions during the photocatalytic reaction. The improvement in the capability of adsorbing water molecules by dispersing Pt and CFO on b-CN or NSCN contributed significantly to enhancing the photocatalytic activity.

5. CONCLUSIONS

In the pursuit of designing improved photocatalysts, emphasis is given to hybrid materials prepared by integrating and assimilating the desired qualities of individual semiconductors. p−n heterojunctions are one of the unfailing effective strategies for yielding visible light catalytically active formulations. We conclude that p−n heterojunctions fabricated in the present study between carbon nitride (n-type (b-CN) or exfoliated nanosheets (NSCN)) and calcium ferrite (CFO, p-type) were successful in enhancing the photocatalytic hydrogen yield. Exfoliation of bulk carbon nitride into nanosheets indeed improved its characteristics in terms of improved few-layer morphology, allowing fine dispersion (57%) of CFO and delaying or suppressing the recombination reaction by six times as compared to b-CN, as revealed by FsTAS. Thus, NSCN proved to be a better support as well as photocatalyst and was found to improve the performance of heterojunctions CFO/NSCN, Pt−NSCN, and Pt−CFO/NSCN considerably, as compared to bulk carbon nitride counterparts. All hetero-

https://doi.org/10.1021/acsomega.4c06353
ACS Omega 2024, 9, 40182−40203

junctions (CFO/b-CN, CFO/NSCN, Pt−CFO/b-CN, and Pt−CFO/NSCN) were more active than pure phases. Pt−CFO/NSCN was most active, demonstrated 250 times more activity as compared to bulk carbon nitride and 6.5 times more active than CFO/NSCN. A superior morphology of NSCN, CFO−NSCN strong interactions via oxygen linkages as investigated by XPS and PL, a much lower effective band gap (1.41 eV), favorable band alignment at the interface, enhanced band bending and increased width of shallow trap states in CFO/NSCN, increased lifetime of charge carriers by FsTAS and TRPL, and adsorption of a large number of water molecules from MD calculations were found to be responsible for enhanced photocatalytic hydrogen yield over Pt−CFO/NSCN heterojunctions in the above manuscript.

■ ASSOCIATED CONTENT

Supporting Information

The Supporting Information is available free of charge at https://pubs.acs.org/doi/10.1021/acsomega.4c06353.

Experimental details; synthesis schematic; characterization of b-CN, NSCN, CFO/b-CN, CFO, NSCN, and Pt−CFO/NSCN photocatalysts by XRD, FTIR, SEM, EDX, and XPS survey scan; femtosecond TA spectra of NSCN at different delay times; triexponential fitting of TRPL spectra and parameters derived; theoretical modeling parameters for different photocatalysts; side and top view of the simulation box containing g-C_3N_4 nanosheets; density profiles; and Lennard−Jones (LJ) potential parameters (PDF)

■ AUTHOR INFORMATION

Corresponding Author

Mrinal R. Pai − *Chemistry Division, Bhabha Atomic Research Centre, Mumbai 400085, India; Homi Bhabha National Institute, Mumbai 400085, India;* orcid.org/0000-0002-5243-7971; Phone: 912225592288; Email: mrinalr@barc.gov.in, mrinalpai9@gmail.com

Authors

Rajendra V. Singh − *Chemistry Division, Bhabha Atomic Research Centre, Mumbai 400085, India; Homi Bhabha National Institute, Mumbai 400085, India*

Atindra M. Banerjee − *Chemistry Division, Bhabha Atomic Research Centre, Mumbai 400085, India; Homi Bhabha National Institute, Mumbai 400085, India*

Anshu Shrivastava − *Department of Chemistry, Indian Institute of Technology (Banaras Hindu University), Varanasi 221005, India*

Uttam Kumar − *Department of Chemistry, Indian Institute of Technology (Banaras Hindu University), Varanasi 221005, India;* orcid.org/0000-0001-8327-8857

Indrajit Sinha − *Department of Chemistry, Indian Institute of Technology (Banaras Hindu University), Varanasi 221005, India*

Bijaideep Dutta − *Chemistry Division, Bhabha Atomic Research Centre, Mumbai 400085, India*

Puthussericka A. Hassan − *Chemistry Division, Bhabha Atomic Research Centre, Mumbai 400085, India; Homi Bhabha National Institute, Mumbai 400085, India;* orcid.org/0000-0001-7137-4788

Raghumani S. Ningthoujam − *Chemistry Division, Bhabha Atomic Research Centre, Mumbai 400085, India; Homi Bhabha National Institute, Mumbai 400085, India;* orcid.org/0000-0002-4642-5990

Rajib Ghosh − *Radiation and Photochemistry Division, Bhabha Atomic Research Centre, Mumbai 400085, India*

Sukhendu Nath − *Radiation and Photochemistry Division, Bhabha Atomic Research Centre, Mumbai 400085, India; Homi Bhabha National Institute, Mumbai 400085, India;* orcid.org/0000-0001-9976-7719

Rajendra K. Sharma − *Technical Physics Division, Bhabha Atomic Research Centre, Mumbai 400085, India*

Jagannath − *Technical Physics Division, Bhabha Atomic Research Centre, Mumbai 400085, India*

Rudheer D. Bapat − *Department of Condensed Matter Physics and Materials Science, Tata Institute of Fundamental Research, Mumbai 400005, India*

Complete contact information is available at: https://pubs.acs.org/10.1021/acsomega.4c06353

Notes

The authors declare no competing financial interest.

■ ACKNOWLEDGMENTS

The authors thank SAIF, IIT Bombay for recording HRTEM and HAADF images. Analytical Chemistry Division, BARC, is sincerely acknowledged for chemical composition analysis by ICP-OES and CHN. The authors acknowledge Dr. A.K. Tripathi, ex-Head, HECS, Chemistry Division, BARC, for his keen support and encouragement.

■ REFERENCES

(1) Staffell, I.; Scamman, D.; Abad, A. V.; Balcombe, P.; Dodds, P. E.; Ekins, P.; Shah, N.; Ward, K. R. The role of hydrogen and fuel cells in the global energy system. *Energy Environ. Sci.* **2019**, *12*, 463−491.

(2) Fujishima, A.; Honda, K. Electrochemical Photolysis of Water at a Semiconductor Electrode. *Nature* **1972**, *238*, 37−38.

(3) Truppi, A.; Petronella, F.; Placido, T.; Margiotta, V.; Lasorella, G.; Giotta, L.; Giannini, C.; Sibillano, T.; Murgolo, S.; Mascolo, G.; Agostiano, A.; Curri, M. L.; Comparelli, R. Gram-scale synthesis of UV−vis light active plasmonic photocatalytic nanocomposite based on TiO_2/Au nanorods for degradation of pollutants in water. *Appl. Catal., B.* **2019**, *243*, 604−613.

(4) Ju, L.; Dai, Y.; Wei, W.; Li, M.; Liang, Y.; Huang, B. One-dimensional cadmium sulphide nanotubes for photocatalytic water splitting. *Phys. Chem. Chem. Phys.* **2018**, *20*, 1904−1913.

(5) Chen, S.; Ma, G.; Wang, Q.; Sun, S.; Hisatomi, T.; Higashi, T.; Wang, Z.; Nakabayashi, M.; Shibata, N.; Pan, Z.; Hayashi, T.; Minegishi, T.; Takata, T.; Domen, K. Metal selenide photocatalysts for visible-light-driven Z-scheme pure water splitting. *J. Mater. Chem. A* **2019**, *7*, 7415−7422.

(6) Maeda, K.; Teramura, K.; Lu, D.; Takata, T.; Saito, N.; Inoue, Y.; Domen, K. Photocatalyst releasing hydrogen from water. *Nature* **2006**, *440*, No. 295.

(7) Guan, X.; Chowdhury, F. A.; Pant, N.; Guo, L.; Vayssieres, L.; Mi, Z. Efficient Unassisted Overall Photocatalytic Seawater Splitting on GaN-Based Nanowire Arrays. *J. Phys. Chem. C* **2018**, *122* (25), 13797−13802.

(8) Zhao, C.; Luo, H.; Chen, F.; Zhang, P.; Yi, L.; You, K. A novel composite of TiO_2 nanotubes with remarkably high efficiency for hydrogen production in solar-driven water splitting. *Energy Environ. Sci.* **2014**, *7*, 1700−1707.

(9) Yuan, Y.-J.; Shen, Z.; Wu, S.; Su, Y.; Pei, L.; Ji, Z.; Ding, M.; Bai, W.; Chen, Y.; Yu, Z.-T.; Zou, Z. Liquid exfoliation of g-C_3N_4 nanosheets to construct 2D-2D MoS_2/g-C_3N_4 photocatalyst for enhanced photocatalytic H_2 production activity. *Appl. Catal., B* **2019**, *246*, 120−128.

(10) Rajendran, S.; Mani, S. S.; Nivedhitha, T. R.; Asoka, A. K.; Arun, P. S.; Mathew, T.; Gopinath, C. S. Facile One-Pot Synthesis of Cu_xO/TiO_2 Photocatalysts by Regulating Cu Oxidation State for Efficient Solar H_2 Production. *ACS Appl. Energy Mater.* **2024**, *7* (1), 104−116.
(11) Rawool, S. A.; Pai, M. R.; Banerjee, A. M.; Bapat, R. D.; Nayak, C.; Tripathi, A. K. Lab scale optimization of various factors for photocatalytic hydrogen generation over low cost $Cu_{0.02}Ti_{0.98}O_{2-\delta}$ photocatalyst under UV/Visible irradiation and sunlight. *Int. J. Hydrogen Energy.* **2018**, *43* (3), 1271−1284.
(12) Ismael, M.; Wu, Y. A mini-review on the synthesis and structural modification of g-C_3N_4-based materials, and their applications in solar energy conversion and environmental remediation. *Sustainable Energy Fuels* **2019**, *3*, 2907−2925.
(13) Wang, X.; Maeda, K.; Thomas, A.; Takanabe, K.; Xin, G.; Carlsson, J. M.; Domen, K.; Antonietti, M. A metal-free polymeric photocatalyst for hydrogen production from water under visible light. *Nat. Mater.* **2009**, *8*, 76−80.
(14) Wang, Y.; Li, Y.; Ju, W.; Wang, J.; Yao, H.; Zhang, L.; Wang, J.; Li, Z. Molten salt synthesis of water-dispersible polymeric carbon nitride nanoseaweeds and their application as luminescent probes. *Carbon* **2016**, *102*, 477−486.
(15) Cui, Y.; Ding, Z.; Fu, X.; Wang, X. Construction of conjugated carbon nitride nanoarchitectures in solution at low temperatures for photoredox catalysis. *Angew. Chem., Int. Ed.* **2012**, *51*, 11814−11818.
(16) Wang, Y.; Wang, X.; Antonietti, M. Polymeric graphitic carbon nitride as a heterogeneous organocatalyst: From photochemistry to multipurpose catalysis to sustainable chemistry. *Angew. Chem., Int. Ed.* **2012**, *51*, 68−89.
(17) Liu, Y.; Sun, Y.; Zhao, E.; Yang, W.; Lin, J.; Zhong, Q.; Qi, H.; Deng, A.; Yang, S.; Zhang, H.; He, H.; Liu, S.; Chen, Z.; Wang, S. Atomically Dispersed Silver-Cobalt Dual-Metal Sites Synergistically Promoting Photocatalytic Hydrogen Evolution. *Adv. Funct. Mater.* **2023**, *33*, No. 2301840.
(18) Nasir, M. S.; Yang, G.; Ayub, I.; Wang, S.; Wang, L.; Wang, X.; Yan, W.; Peng, S.; Ramakarishna, S. Recent development in graphitic carbon nitride based photocatalysis for hydrogen generation. *Appl. Catal., B* **2019**, *257*, No. 117855.
(19) Liu, Y.; Xu, X.; Zhang, J.; Zhang, H.; Tian, W.; Li, X.; Tade, M. O.; Sun, H.; Wang, S. Flower-like MoS_2 on graphitic carbon nitride for enhanced photocatalytic and electrochemical hydrogen evolutions. *Appl. Catal., B* **2018**, *239*, 334−344.
(20) Wu, X.; Ma, H.; Zhong, W.; Fan, J.; Yu, H. Porous crystalline g-C_3N_4: Bifunctional $NaHCO_3$ template-mediated synthesis and improved photocatalytic H_2-evolution rate. *Appl. Catal., B* **2020**, *271*, No. 118899.
(21) Wen, J.; Xie, J.; Chen, X.; Li, X. A review on g-C_3N_4 -based photocatalysts. *Appl. Surf. Sci.* **2017**, *391*, 72−123.
(22) Kim, J. S.; Oh, J. W.; Woo, S. I. Investigation for the effects of ball milling process on the physical characteristics, the behaviors of carriers and the photocatalytic activity of sulfur doped g-C_3N_4. *Int. J. Hydrogen Energy* **2017**, *42*, 5485−5495.
(23) Wang, H.; Zhang, L.; Chen, Z.; Hu, J.; Li, S.; Wang, Z.; Liu, J.; Wang, X. Semiconductor Heterojunction Photocatalysts: Design, Construction, and Photocatalytic Performances. *Chem. Soc. Rev.* **2014**, *43*, 5234−5244.
(24) Sathish, M.; Viswanathan, B.; Viswanath, R. P. Alternate Synthetic Strategy for the Preparation of CdS Nanoparticles and its Exploitation for Water Splitting. *Int. J. Hydrogen Energy* **2006**, *31*, 891−898.
(25) Ong, W.-J.; Tan, L.-L.; Ng, Y. H.; Yong, S.-T.; Chai, S.-P. Graphitic carbon Nitride (g-C_3N_4) Based Photocatalysts for Artificial Photosynthesis and Environmental Remediation: Are We A Step Closer to Achieving Sustainability? *Chem. Rev.* **2016**, *116*, 7159−7329.
(26) Zhao, Z.; Sun, Y.; Dong, F. Graphitic carbon nitride-based nanocomposites: a review. *Nanoscale* **2015**, *7*, 15−37.
(27) Deng, A.; Sun, Y.; Gao, Z.; Yang, S.; Liu, Y.; He, H.; Zhang, J.; Liu, S.; Sun, H.; Wang, S. Internal electric field in carbon nitride-based heterojunctions for photocatalysis. *Nano Energy* **2023**, *108*, No. 108228.
(28) Kheradmand, A.; Wainwright, A.; Wang, L.; Jiang, Y. Anchoring Iron Oxides on Carbon Nitride Nanotubes for Improved Photocatalytic Hydrogen Production. *Energy Fuels* **2021**, *35* (1), 868−876.
(29) Kumar, S. G.; Kavitha, R.; Manjunatha, C. Review and Perspective on Rational Design and Interface Engineering of g-C_3N_4/ZnO: From Type-II to Step-Scheme Heterojunctions for Photocatalytic Applications. *Energy Fuels* **2023**, *37* (19), 14421−14472.
(30) Fiqar, Z.; Tao, J.; Yang, T.; Liu, Q.; Hu, J.; Tang, H. Designing 0D/2D CdS nanoparticles/g-C_3N_4 nanosheets heterojunction as efficient photocatalyst for improved H_2-evolution. *Surf. Interfaces* **2021**, *26*, No. 101312.
(31) Zhang, B.; Shi, H.; Yan, Y.; Liu, C.; Hu, X.; Liu, E.; Fan, J. A novel S-scheme 1D/2D Bi_2S_3/g-C_3N_4 heterojunctions with enhanced H_2 evolution activity. *Colloids Surf., A* **2021**, *608*, No. 125598.
(32) Chen, Y.; Wang, Q.; Huang, H.; Kou, J.; Lu, C.; Xu, Z. Effective solar driven H_2 production by $Mn_{0.5}Cd_{0.5}Se$/g-C_3N_4 S-scheme heterojunction photocatalysts. *Int. J. Hydrogen Energy* **2021**, *46*, 32514−32522.
(33) She, X.; Wu, J.; Xu, H.; Zhong, J.; Wang, Y.; Song, Y.; Nie, K.; Liu, Y.; Yang, Y.; Rodrigues, M.-T.; Vajtai, R.; Lou, J.; Du, D.; Li, H.; Ajayan, P. High efficiency photocatalytic water splitting using 2D alpha-Fe_2O_3/g-C_3N_4 Z-scheme catalysts. *Adv. Energy Mater.* **2017**, *7*, No. 1700025.
(34) Rawool, S. A.; Pai, M. R.; Banerjee, A. M.; Nath, S.; Bapat, R. D.; Sharma, R. K.; Jagannath; Dutta, B.; Hassan, P. A.; Tripathi, A. K. Superior Interfacial Contact Yields Efficient Electron Transfer Rate and Enhanced Solar Photocatalytic Hydrogen Generation in M/C_3N_4 Schottky Junctions. *ACS Appl. Mater. Interfaces* **2023**, *15*, 39926−39945.
(35) Rawool, S. A.; Pai, M. R.; Banerjee, A. M.; Arya, A.; Ningthoujam, R. S.; Tewari, R.; Rao, R.; Chalke, B.; Ayyub, P.; Tripathi, A. K.; Bharadwaj, S. R. pn Heterojunctions in NiO:TiO_2 composites with type-II band alignment assisting sunlight driven photocatalytic H_2 generation. *Appl. Catal., B* **2018**, *221*, 443−458.
(36) Ida, S.; Yamada, K.; Matsunaga, T.; Hagiwara, H.; Matsumoto, Y.; Ishihara, T. Preparation of p-type $CaFe_2O_4$ photocathodes for producing hydrogen from water. *J. Am. Chem. Soc.* **2010**, *132*, 17343−17345.
(37) Matsumoto, Y.; Obata, M.; Hombo, J. Photocatalytic reduction of carbon dioxide on p-type $CaFe_2O_4$ powder. *J. Phys. Chem. A* **1994**, *98*, 2950−2951.
(38) Zhang, F.; Fang, Z. Hydrolysis of cellulose to glucose at the low temperature of 423 K with $CaFe_2O_4$-based solid catalyst. *Bioresour. Technol.* **2012**, *124*, 440−445.
(39) Tsipis, E. V.; Pivak, Y. V.; Waerenborgh, J. C.; Kolotygin, V. A.; Viskup, A. P.; Kharton, V. V. Oxygen ionic conductivity, Mössbauer spectra and thermal expansion of $CaFe_2O_{4-\delta}$. *Solid State Ionics* **2007**, *178*, 1428−1436.
(40) Vadivel, S.; Maruthamani, D.; Habibi-Yangjeh, A.; Paul, B.; Dhar, S. S.; Selvam, K. Facile synthesis of novel $CaFe_2O_4$/g-C_3N_4 nanocomposites for degradation of methylene blue under visible-light irradiation. *J. Colloid Interface Sci.* **2016**, *480*, 126−136.
(41) Shenoy, S.; Chuaicham, C.; Okumura, T.; Sekar, K.; Sasaki, K. Simple tactic polycondensation synthesis of Z-scheme quasi-polymeric g-C_3N_4/$CaFe_2O_4$ composite for enhanced photocatalytic water depollution via p-n heterojunction. *Chem. Eng. J.* **2023**, *453*, No. 139758.
(42) Liu, F.; Dong, S.; Zhang, Z.; Li, X.; Dai, X.; Xin, Y.; Wang, X.; Liu, K.; Yuan, Z.; Zheng, Z. Synthesis of a well-dispersed $CaFe_2O_4$/g-C_3N_4/CNT composite towards the degradation of toxic water pollutants under visible light. *RSC Adv.* **2019**, *9*, 25750−25761.
(43) Das, K. K.; Patnaik, S.; Mansingh, S.; Behera, A.; Mohanty, A.; Acharya, C.; Parida, K. M. Enhanced photocatalytic activities of polypyrrole sensitized zinc ferrite/graphitic carbon nitride n-n heterojunction towards ciprofloxacin degradation, hydrogen evolution and antibacterial studies. *J. Colloid Interface Sci.* **2020**, *561*, 551−567.
(44) Mehtab, A.; Banerjee, S.; Mao, Y.; Ahmad, T. Type-II $CuFe_2O_4$/Graphitic Carbon Nitride Heterojunctions for High-Efficiency Photocatalytic and Electrocatalytic Hydrogen Generation. *ACS Appl. Mater. Interfaces* **2022**, *14* (39), 44317−44329.

https://doi.org/10.1021/acsomega.4c06353
ACS Omega 2024, 9, 40182−40203

(45) Aksoy, M.; Yanalak, G.; Aslan, E.; Patır, I. H.; Metin, Ö. Visible light-driven hydrogen evolution by using mesoporous carbon nitride-metal ferrite (MFe_2O_4/mpg-CN; M: Mn, Fe, Co and Ni) nanocomposites as catalysts. *Int. J. Hydrogen Energy* **2020**, *45*, 16509−16518.
(46) Belakehal, R.; Atacan, K.; Güy, N.; Megriche, A.; Özacar, M. Fabrication of heterostructured CdS/g-C_3N_4/$ZnFe_2O_4$ nanocomposite synthesized through ultrasonic-assisted method for efficient photocatalytic hydrogen production. *Appl. Surf. Sci.* **2022**, *602*, No. 154315.
(47) Chen, J.; Zhao, D.; Diao, Z.; Wang, M.; Shen, S. Ferrites boosting photocatalytic hydrogen evolution over graphitic carbon nitride: a case study of (Co, Ni)Fe_2O_4 modification. *Sci. Bull.* **2016**, *61*, 292−301.
(48) Cosic, I.; Cosic, D.; Lazar, K. Environmental Light and Its Relationship with Electromagnetic Resonances of Biomolecular Interactions, as Predicted by the Resonant Recognition Model. *Int. J. Environ. Res. Public Health* **2016**, *13*, No. 647.
(49) Pai, M. R.; Majeed, J.; Banerjee, A. M.; Arya, A.; Bhattacharya, S.; Rao, R.; Bharadwaj, S. R. Role of Nd^{3+} ions in modifying the band structure and photocatalytic properties of substituted indium titanates, $In_{2(1-x)}Nd_{2x}TiO_5$ oxides. *J. Phys. Chem. C* **2012**, *116*, 1458−1471.
(50) Hak, C. H.; Sim, L. C.; Leong, K. H.; Lim, P. F.; Chin, Y. H.; Saravanan, P. M/g-C_3N_4 (M = Ag, Au, and Pd) composite: synthesis via sunlight photodeposition and application towards the degradation of bisphenol A. *Environ. Sci. Pollut. Res.* **2018**, *25*, 25401−25412.
(51) Tong, J.; Zhang, L.; Li, F.; Wang, K.; Han, L.; Cao, S. Rapid and high-yield production of g-C_3N_4 nanosheets via chemical exfoliation for photocatalytic H_2 evolution. *RSC Adv.* **2015**, *5*, 88149−88153.
(52) Šutka, A.; Kodu, M.; Pärna, R.; Saar, R.; Juhnevica, I.; Jaaniso, R.; Kisand, V. Orthorhombic $CaFe_2O_4$: A promising p-type gas sensor. *Sens. Actuators, B* **2016**, *224*, 260−265.
(53) Huang, J.; Klahn, M.; Tian, X.; Dai, X.; Rabeah, J.; Aladin, V.; Corzilius, B.; Bartling, S.; Lund, H.; Steinfeldt, N.; Peppel, T.; Logsdail, A. J.; Jiao, H.; Strunk, J. Exfoliated Polymeric Carbon Nitride Nanosheets for Photocatalytic Applications. *ACS Appl. Nano Mater.* **2024**, *7*, 7442−7452.
(54) Maluangnont, T.; Pulphol, P.; Chaithaweep, K.; Dabsamut, K.; Kobkeatthawin, T.; Smith, S. M.; Boonchun, A.; Vittayakornc, N. Alternating current properties of bulk- and nanosheet-graphitic carbon nitride compacts at elevated temperatures. *RSC Adv.* **2023**, *13* (36), 25276−25283.
(55) Zhang, L.; Wang, H.; Shen, W.; Qin, Z.; Wang, J.; Fan, W. Controlled synthesis of graphitic carbon nitride and its catalytic properties in Knoevenagel condensations. *J. Catal.* **2016**, *344*, 293−302.
(56) Lei, D.; Xue, J.; Peng, X.; Li, S.; Bi, Q.; Tang, C.; Zhang, L. Oxalate enhanced synergistic removal of chromium(VI) and arsenic-(III) over $ZnFe_2O_4$/g-C_3N_4: Z scheme charge transfer pathway and photo-Fenton like reaction. *Appl. Catal., B* **2021**, *282*, No. 119578.
(57) Lau, V. W. H.; Mesch, M. B.; Duppel, V.; Blum, V.; Senker, J.; Lotsch, B. V. Low-Molecular-Weight Carbon Nitrides for Solar Hydrogen Evolution. *J. Am. Chem. Soc.* **2015**, *137*, 1064−1072.
(58) Sato, S.; Kataoka, K.; Jinnouchi, R.; Takahashi, N.; Sekizawa, K.; Kitazumi, K.; Ikenaga, E.; Asahi, R.; Morikawa, T. Band bending and dipole effect at interface of metal-nanoparticles and TiO_2 directly observed by angular-resolved hard X-ray photoemission spectroscopy. *Phys. Chem. Chem. Phys.* **2018**, *20*, 11342−11346.
(59) Bhosale, R.; Jain, S.; Vinod, C. P.; Kumar, S.; Ogale, S. Direct Z-Scheme g-C_3N_4/$FeWO_4$ nanocomposite for enhanced and selective photocatalytic CO_2 reduction under visible light. *ACS Appl. Mater. Interfaces* **2019**, *11*, 6174−6183.
(60) Zhang, Z.; Liu, K.; Feng, Z.; Bao, Y.; Dong, B. Hierarchical Sheet-on-Sheet $ZnIn_2S_4$/g-C_3N_4 Heterostructure with Highly Efficient Photocatalytic H_2 production Based on Photoinduced Interfacial Charge Transfer. *Sci. Rep.* **2016**, *6*, No. 19221.
(61) Veldurthi, N. K.; Eswar, N. K.; Singh, S. A.; Madras, G. Cooperative effect between $BaTiO_3$ and $CaFe_2O_4$ in a cocatalyst-free heterojunction composite for improved photochemical H_2 generation. *Int. J. Hydrogen Energy.* **2018**, *43*, 22929−22941.
(62) Yamashita, T.; Hayes, P. Analysis of XPS spectra of Fe^{2+} and Fe^{3+} ions in oxide materials. *Appl. Surf. Sci.* **2008**, *254*, 2441−2449.
(63) Zhang, W.; Yao, Q.; Jiang, G.; Li, C.; Fu, Y.; Wang, X.; Yu, A.; Chen, Z. Molecular trapping strategy to stabilize subnanometric Pt clusters for highly active electrocatalysis. *ACS Catal.* **2019**, *9* (12), 11603−11613.
(64) Jang, J. S.; Choi, S. H.; Kim, H. G.; Lee, J. S. Location and State of Pt in Platinized CdS/TiO_2 Photocatalysts for Hydrogen Production from Water under Visible Light. *J. Phys. Chem. C* **2008**, *112* (44), 17200−17205.
(65) Zhang, Y.; Pan, Q.; Chai, G.; Liang, M.; Dong, G.; Zhang, Q.; Qiu, J. Synthesis and Luminescence Mechanism of Multicolor-emitting g-C_3N_4 Nanopowders by Low Temperature Thermal Condensation of Melamine. *Sci. Rep.* **2013**, *3*, No. 1943.
(66) Yaghoubi, H.; Li, Z.; Chen, Y.; Ngo, H. T.; Bhethanabotla, V. R.; Joseph, B.; Ma, S.; Schlaf, R.; Takshi, A. Toward a visible light-driven photocatalyst: The effect of midgap-states-induced energy gap of undoped TiO_2 nanoparticles. *ACS Catal.* **2015**, *5*, 327−335.
(67) Xue, J.; Fujitsuka, M.; Majima, T. Shallow Trap State-Induced Efficient Electron Transfer at the Interface of Heterojunction Photocatalysts: The Crucial Role of Vacancy Defects. *ACS Appl. Mater. Interfaces* **2019**, *11*, 40860−40867.
(68) Godin, R.; Wang, Y.; Zwijnenburg, M. A.; Tang, J.; Durrant, J. R. Time-Resolved Spectroscopic Investigation of Charge Trapping in Carbon Nitrides Photocatalysts for Hydrogen Generation. *J. Am. Chem. Soc.* **2017**, *139*, 5216−5224.
(69) Shi, H.; Long, S.; Hou, J.; Ye, L.; Sun, Y.; Ni, W.; Song, C.; Li, K.; Gurzadyan, G. G.; Guo, X. Defects Promote Ultrafast Charge Separation in Graphitic Carbon Nitride for Enhanced Visible-Light-Driven CO_2 Reduction Activity. *Chem. - Eur. J.* **2019**, *25*, 5028−5035.
(70) Xue, J.; Fujitsuka, M.; Majima, T. Near Bandgap Excitation Inhibits the Interfacial Electron Transfer of Semiconductor/Cocatalyst. *ACS Appl. Mater. Interfaces* **2020**, *12*, 5920−5924.
(71) Murthy, D. H. K.; Matsuzaki, H.; Wang, Z.; Suzuki, Y.; Hisatomi, T.; Seki, K.; Inoue, Y.; Domen, K.; Furube, A. Origin of the Overall Water Splitting Activity of Ta_3N_5 Revealed by Ultrafast Transient Absorption Spectroscopy. *Chem. Sci.* **2019**, *10*, 5353−5362.
(72) Niu, P.; Zhang, L.; Liu, G.; Cheng, H.-M. Graphene-Like Carbon Nitride Nanosheets for Improved Photocatalytic Activities. *Adv. Funct. Mater.* **2012**, *22* (22), 4763−4770.
(73) Karim, K. M. R.; Tarek, M.; Sarkar, S. M.; Mouras, R.; Ong, H. R.; Abdullah, H.; Cheng, C. K.; Khan, M. M. R. Photoelectrocatalytic reduction of CO_2 to methanol over $CuFe_2O_4$@PANI photocathode. *Int. J. Hydrogen Energy.* **2021**, *46* (48), 24709−24720.
(74) Kumar, U.; Shrivastava, A.; De, A. K.; Pai, M. R.; Sinha, I. Fenton Reaction by H_2O_2 Produced on a Magnetically Recyclable Ag/$CuWO_4$/$NiFe_2O_4$ Photocatalyst. *Catal. Sci. Technol.* **2023**, *13*, 2432−2446.
(75) Sarkar, R.; Kundu, T. K. Hydrogen Bond Interactions of Hydrated Aluminum Nitrate with PVDF, PVDF-TrFE, and PVDF-HFP: A Density Functional Theory-Based Illustration. *Int. J. Quantum Chem.* **2020**, *120* (17), No. e26328.
(76) Acharya, R.; Pati, S.; Parida, K. A review on visible light driven spinel ferrite-g-C_3N_4 photocatalytic systems with enhanced solar light utilization. *J. Mol. Liq.* **2022**, *357*, No. 119105.
(77) Guo, S.; Yang, Z.; Zhang, H.; Yang, W.; Li, J.; Zhou, K. Enhanced photocatalytic degradation of organic contaminants over $CaFe_2O_4$ under visible LED light irradiation mediated by peroxymonosulfate. *J. Mater. Sci. Technol.* **2021**, *62*, 34−43.

https://doi.org/10.1021/acsomega.4c06353
ACS Omega 2024, 9, 40182−40203